


# Modeling of cavity nucleation, early-stage growth, and sintering in polycrystal under creep–fatigue interaction

Jingdong Hu<sup>1,2,3</sup> | Changjun Liu<sup>1</sup> | Fuzhen Xuan<sup>1</sup> | Bo Chen<sup>2</sup> 

<sup>1</sup>Key Laboratory of Pressure Systems and Safety, Ministry of Education, School of Mechanical and Power Engineering, East China University of Science and Technology, Shanghai, China

<sup>2</sup>School of Engineering, University of Leicester, Leicester, UK

<sup>3</sup>Shanghai Nuclear Engineering Research and Design Institute, Shanghai, China

## Correspondence

Jingdong Hu, Key Laboratory of Pressure Systems and Safety, Ministry of Education, School of Mechanical and Power Engineering, East China University of Science and Technology, Shanghai 200237, China.

Email: jh788@leicester.ac.uk

Bo Chen, School of Engineering, University of Leicester, Leicester LE1 7RH, UK.

Email: bo.chen@leicester.ac.uk

## Funding information

China Scholarship Council (CSC), Grant/Award Number: 201906740075; EPSRC Early Career Fellowship Scheme, Grant/Award Number: EP/R043973/1; East China University of Science and Technology

## Abstract

A mechanistic-based cavitation model that considers nucleation, early-stage growth, and sintering under creep–fatigue interaction is proposed to predict the number density of cavities  $\rho$ . Both the nucleation and early-stage growth rates, controlled by grain boundary (GB) sliding under tension, are formulated as a function of local normal stress  $\sigma_n$ . Cavity sintering that occurs during the compression is governed by the unconstrained GB diffusion depending on the  $\sigma_n$ . Modeling results provide important insights into experimental load-waveform design. First, test with initial compression promotes higher  $\rho$  compared to the initial tension, if the unbalanced hold time in favor of tension is satisfied. Second, the  $\rho$  value does not have a monotonic dependence on either the compressive hold time or stress, because of their competing effect on nucleation and sintering. Third, the optimum value of stress variation rate exists in terms of obtaining the highest  $\rho$  value due to sintering effect.

## KEYWORDS

analytic solutions, cavity, cavity sintering, creep, viscoplastic

## 1 | INTRODUCTION

Creep-dominated creep–fatigue interaction is a long-term material failure mode that involves cyclic loading.<sup>1</sup> Lack of fundamental understanding on this topic prevents us to commercialize the Generation IV high-temperature nuclear power plants with a design life of 60 years.<sup>2</sup> Although the mechanistic-based descriptions of cavity nucleation, growth, and coalescence under

creep have been established,<sup>3</sup> little attempt have been made to reveal the mechanism of cavity nucleation and its early-stage radius change under creep–fatigue interaction.<sup>4,5</sup>

The empirical relationship between cavity nucleation rate under creep and Monkman–Grant constant has been established by Davanas,<sup>6</sup> providing a good agreement with experimental data. But it is unclear about its suitability for creep–fatigue interaction. Cavitation under

This is an open access article under the terms of the Creative Commons Attribution License, which permits use, distribution and reproduction in any medium, provided the original work is properly cited.

© 2022 The Authors. *Fatigue & Fracture of Engineering Materials & Structures* published by John Wiley & Sons Ltd.

fatigue is known to be different from that under creep, in a sense that fatigue-induced cavities are smaller in size but higher in their number density.<sup>5</sup> There are creep-fatigue lifetime prediction models that consider the creep cavitation mechanism, for example, Nam.<sup>7</sup> However, the model cannot explain the positive relationship between the cavity nucleation and tensile hold time.<sup>8</sup> Recent work by Wen et al.<sup>9</sup> and Barbera et al.<sup>10</sup> used creep damage models to predict crack growth rate under creep-fatigue, by incorporating the late-stage cavity growth. However, they did not consider the physical process of cavity nucleation or early-stage growth.

Moreover, little knowledge has been gained regarding the cavity sintering. Compressive loading can cause the nucleated creep cavities shrink in radius and forces them to be removed completely under some circumstances.<sup>11,12</sup> This means that their number density after certain number of cycles is not the simple sum of nucleated cavities from each cycle. To the best of the authors' knowledge, creep cavitation model considering both the nucleation and sintering events under creep-fatigue interaction does not exist so far.

The mechanism of cavity nucleation was initially proposed by Greenwood<sup>13</sup> and developed further by Raj and Ashby.<sup>14</sup> It has been accepted that vacancies agglomerate and form stable nuclei assisted by local normal stress. The local normal stress can be significantly higher than the far-field stress.<sup>15</sup> One of the causes is grain boundary (GB) sliding induced stress concentration. Extensive cavitation was found in copper bicrystals which had been subjected to prestrain in favor of GB sliding followed by creep loading.<sup>16,17</sup> Min and Raj<sup>18</sup> proposed a model to predict the local normal stress under creep-fatigue loading based on the GB sliding mechanism. By considering the creep effect on local normal stress, our model is capable of predicting the cavity nucleation under one-cycle creep-fatigue.<sup>19</sup>

Modeling the early-stage radius change is key to understanding the sintering process under creep-fatigue. Note that sintering shares a high degree of commonality with the cavity growth. The classical growth models were established under either or both of vacancy diffusion and matrix deformation,<sup>20–24</sup> and the growth rate is controlled by the far-field stress. Nevertheless, these models might not be suitable for the early-stage growth. First, the radius of nucleated cavities ( $\sim 5$  nm) is much smaller than those commonly defined “small” cavities ( $\sim 1$   $\mu\text{m}$ ).<sup>3</sup> This indicates that the vacancy flow near the cavities is highly sensitive to the local normal stress.<sup>25</sup> Second, the cavity-growth mechanism map<sup>26</sup> does not consider the role of GB sliding on the early-stage growth, despite its importance.<sup>25</sup>

In this paper, the number density of cavities and their time evolution during multicycle creep-fatigue loading are modeled. The stress-controlled load waveform is considered because a higher creep damage would be generated in comparison with the strain-controlled one.<sup>27,28</sup> Type 316 stainless steel is selected for twofold reasons: Material parameters are available<sup>18,29–31</sup> and its wide application to the power generation industry.<sup>2,29</sup>

## 2 | MODELING APPROACH

### 2.1 | Theoretical modeling

Modeling cavitation under creep-fatigue contains two parts. The first part focuses on describing the relationship between the applied stress and local normal stress and the cavity nucleation governed by vacancy accumulation. This part is based on the classical nucleation theory that describes nucleation under high stress level.<sup>3</sup> The second part concerns about the radius change of nucleated cavities during creep-fatigue loading. These two parts are integrated through a numerical framework to give the final prediction to the number density of cavities. The governing equations are described below.

The rate of cavity nucleation ( $\dot{\rho}$ ) on the particles at GB can be described as<sup>14</sup>

$$\dot{\rho} = (\rho_{\max} - \rho) \exp \left[ - \left( \frac{4\gamma^3 F_v}{\sigma_n^2 kT} \right) \right] \frac{4\pi\gamma}{\Omega^{4/3} \sigma_n} \delta D_B \left( 1 + \frac{\sigma_n \Omega}{kT} \right), \quad (1)$$

where  $\Omega$  is the atomic volume and  $k$  is the Boltzmann constant.  $\delta D_B$  is the GB thickness multiplied by its self-diffusion coefficient.  $\gamma$  is the free surface energy.  $F_v$  is a shape factor related to the cavity volume, and it has a value of 0.1585 for cavity nucleation at the top of GB particles.<sup>14</sup>  $\rho_{\max}$  is the maximum number density of potential nucleation sites, and its value can be worked out through the relation of  $(4\sqrt{3}f_b/3d\bar{p}) \times 10^6$  by Wang et al.,<sup>32</sup> by assuming that the grain has an idealized hexagonal shape.  $f_b$  is the area fraction of GB particles,  $\bar{p}$  is their average radius (in  $\mu\text{m}$ ), and  $d$  is the grain size (in  $\mu\text{m}$ ). The coefficient of  $10^6$  is the consequence of expressing the number density of cavities in  $\text{mm}^{-2}$ .

The cavity nucleation rate  $\dot{\rho}$  in Equation 1 depends on three variables: number density of nucleated cavities, local normal stress, and temperature, symbolized as  $\rho$ ,  $\sigma_n$ , and  $T$ , respectively. Accordingly, the relationship between the local normal stress and applied shear stress is formulized as follows:

$$\lim_{\Delta t \rightarrow 0} \left[ \frac{\sigma_n(t + \Delta t) - \sigma_n(t)e^{-\frac{\Delta t}{\tau}}}{1 - e^{-\frac{\Delta t}{\tau}}} \right] = \frac{\dot{\sigma}_s(t)}{f_b} \tau + \frac{\sigma_s(t)}{f_b(1 + \eta'_p/\eta_b)}, \quad (2)$$

where  $\sigma_s(t)$ ,  $\dot{\sigma}_s(t)$ , and  $\sigma_n(t)$  are the applied shear stress, its change rate, and the local normal stress at time  $t$ . The derivation of Equation 2 is described in Appendix A.  $\sigma_n(t + \Delta t)$  is the local normal stress at time  $t + \Delta t$ . Note that  $\Delta t$  is the time interval chosen for the numerical computation that will be described in Section 2.3.  $\tau$  is time constant defined as

$$\frac{1}{\tau} = k_e \left( \frac{1}{\eta_b} + \frac{1}{\eta'_p} \right), \quad (3)$$

where  $\eta_b$  is the damping coefficient of GB sliding.  $k_e$  is the elastic modulus, defined as  $G/[0.57d(1 - \nu)]$ .  $\eta'_p$  is the transient creep damping coefficient that has a form of  $\eta_p/[\sigma_s - f_b\sigma_n]^{n-1}$ .  $G$  and  $\nu$  are shear modulus and Poisson's ratio.  $\eta_p$  is the reciprocal of pre-exponential factor, and  $n$  is the exponent in the Norton power-law creep. More details about the cavity nucleation model can be found in Hu et al.<sup>19</sup>

To obtain the actual size of the nucleated cavities, the radius change rate  $\dot{r}$  needs to be determined during the subsequent loadings. For cavity growth, Chen<sup>25</sup> pointed out that GB sliding played an important role in the early-stage growth. The transient GB sliding activity could immediately wedge open the supercritical nuclei along the particles.<sup>33</sup> According to this “crack sharpening” mechanism, the cavity tip velocity is limited by surface diffusion.<sup>3</sup>

Figure 1A shows a schematic diagram of the cavity nucleation and early-stage growth assisted by GB sliding with a rate of  $\dot{U}_{sb}$ . Because of insufficient surface diffusion, the nucleated cavity tends to form an irregular

crack-like shape. This implies that the growth rate is independent on the cavity radius, given that the process is limited by the vacancy diffusion rate near the cavity tip. Based on the work of Chuang et al.,<sup>23</sup> equations were formulized by Nix et al.<sup>34</sup> to describe cavity-growth rate controlled by the vacancy surface diffusion under low and high stresses:

$$\dot{r} = \min \left[ \frac{\Omega \delta_s D_s}{2kT\gamma^2} \sigma_n^3, \frac{(\delta D_B)^{3/2} \Omega \sigma_n^{3/2}}{2(\delta_s D_s)^{1/2} kTb^{3/2} \gamma^{1/2}} \right], \quad \sigma_n > 0, \quad (4)$$

where  $D_s$  is the surface diffusion coefficient.  $\delta_s$  is the width of surface diffusion, which is related to atom volume  $\Omega$ , through  $\delta_s = \Omega^{1/3}$ .  $b$  is the limiting cavity radius, equaling the half of average cavity spacing,  $\lambda/2$ .<sup>23</sup>  $\lambda$  is the average distance between two nucleation sites, and its value can be estimated as below for an idealized hexagonal grain shape:

$$\lambda \geq \frac{d}{f_b d/\bar{p} + 2}. \quad (5)$$

In the growth model,<sup>34</sup> the cavity has been assumed to have a crack-like shape (Figure 1A). The growth process is driven by the accumulation of vacancies at the cavity tip, leading to the phenomenon similar to a crack-tip continuous extension. Meanwhile, the surface diffusion is marginally faster than GB diffusion under low stress, while the surface diffusivity becomes much higher than that of GB under high stress. Refer to Appendix B for the derivation of stress level that separates the two conditions.

The reason for ignoring the creep effect on the early-stage growth can be justified as follows. The growth mechanism map proposed by Miller et al.<sup>26</sup> informs that the cavity radius change is controlled by unconstrained GB diffusion when the ratio of cavity spacing ( $\lambda$ ) to its diameter ( $2r$ ) is greater than 10. In the case of early-stage

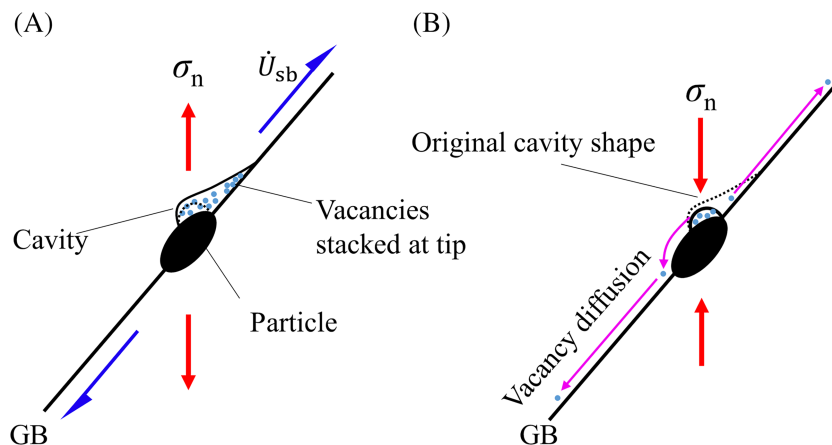


**FIGURE 1** Schematic diagrams of a cavity that (A) grows by the surface diffusion limited GB sliding and (B) shrinks by the unconstrained GB diffusion [Colour figure can be viewed at [wileyonlinelibrary.com](http://wileyonlinelibrary.com)]

cavitation,<sup>3,23</sup> the value of  $\lambda/2r$  falls into the range of 200 to 3000, given that the value range of  $r$  is 3 to 5 nm and that of  $\lambda$  is 1 to 10  $\mu\text{m}$ . Therefore, the unconstrained GB diffusion is the rate-limiting factor for the early-stage growth.

Because of the analogy of shrinkage to growth, shrinkage occurs by the GB vacancy diffusion that pushes vacancies out of the cavity under the compressive  $\sigma_n$ . The reversed direction of GB sliding, coupled with the reduced sharpness of the cavity tip, causes a more uniform distribution of vacancies within the cavity, as shown in Figure 1B. Since the vacancies are no longer concentrated at the tip, more surface areas become the diffusional interface. Ultimately, the cavity shape changes back to sphere, that is the equilibrium shape when the surface diffusion rate is fast enough.<sup>23</sup>

To calculate the shrinkage rate, equation proposed by Riedel<sup>35</sup> for cavity growth under the unconstrained GB diffusion is adapted:

$$\dot{r} = \min \left[ 0, \frac{\Omega \delta D_B (\sigma_n - 2\gamma/r)}{1.22kT \ln(\lambda/4.24r)^2} \right], \quad \sigma_n \leq 0. \quad (6)$$

When the cavity radius  $r$  becomes larger than  $\lambda/4.24$ ,  $\dot{r}$  is set to zero to prevent the unrealistic positive value under compression. This upper limit value has been used to define the largest cavity size. The assumption behind the Riedel model is that cavity is not perfectly spherical, which aligns very well with the considered crack-like cavities. If the cavity radius  $r$  becomes less than the critical nuclei size<sup>14</sup> defined by the value of  $2\gamma/\sigma_n$ , cavities are considered as sintered.<sup>12,36</sup>

TABLE 1 Material parameters in the proposed cavity nucleation and sintering model for Type 316 stainless steel

Parameter	Symbol	Value	Unit	Temperature range (°C)	References
Average radius of the particle at GB	$\bar{p}$	1.0	$\mu\text{m}$	-	Min and Raj <sup>18</sup>
Average size of grains	$d$	40	$\mu\text{m}$	-	Min and Raj <sup>18</sup>
Shear modulus	$G$	$7.6 \times 10^{10}$	Pa	-	Min and Raj <sup>18</sup>
Poisson's ratio	$\nu$	0.31	-	-	Min and Raj <sup>18</sup>
Atom volume	$\Omega$	$1.21 \times 10^{-29}$	$\text{m}^3$	-	Min and Raj <sup>18</sup>
Area fraction of the particles	$f_b$	0.2	-	-	Min and Raj <sup>18</sup>
Shape factor related to the cavity volume	$F_v$	0.1585	-	-	Raj and Ashby <sup>14</sup>
Free surface formation energy	$\gamma$	0.80	$\text{J m}^{-2}$	-	Mortimer and Nicholas <sup>31</sup>
Boltzmann constant	$k$	$1.3806 \times 10^{-23}$	$\text{J K}^{-1}$	-	Universal constant
Gas constant	$R$	8.314	$\text{J mol}^{-1} \text{K}^{-1}$	-	Universal constant
GB diffusion activation energy	$Q_c$	$167 \times 10^3$	$\text{J mol}^{-1}$	-	Frost and Ashby <sup>30</sup>
GB thickness multiplied by its self-diffusion coefficient	$\delta D_B$	$2.0 \times 10^{-13} \exp(-Q_c/RT)$	$\text{m}^3 \text{s}^{-1}$	-	Frost and Ashby <sup>30</sup>
Free surface diffusion coefficient <sup>a</sup>	$D_S$	$9.0 \times 10^{-7} \exp(-167 \times 10^3/RT)$	$\text{m}^2 \text{s}^{-1}$	500–600	Not available in literature
Creep exponent	$n$	11.83	-	500–600	Chen et al. <sup>29</sup>
Pre-exponential factor	$1/\eta_p$	$2.199 \times 10^{-32}$ $8.754 \times 10^{-32}$ $6.489 \times 10^{-31}$ $3.035 \times 10^{-30}$ $2.005 \times 10^{-29}$	$\text{h}^{-1} \text{MPa}^{-n}$	500 525 550 575 600	Chen et al. <sup>29</sup>

<sup>a</sup>Value has been calculated through the relation of  $\delta_S D_S / \delta D_B = 0.001$ .



## 2.2 | Material parameters and temperature effect

Except for the surface diffusion factor  $D_S$ , all the material parameters have been sourced from the authoritative literature listed in Table 1.  $D_S$  values in the temperature range of 500°C to 600°C are not available; hence, the diffusivity ratio of  $\delta_S D_S / \delta D_B = 0.001$  has been used for calculations. This meets the criterion of  $\delta_S D_S / \delta D_B \ll 1$  for a crack-like cavity.<sup>34</sup> Justification of the  $D_S$  value selection through a sensitivity study is described in Appendix B. In this context, our model has been established based on the state-of-the-art mechanistic understanding of cavitation and the prediction results are reliable (no approximation or extrapolation).

Creep database for Type 316H stainless steel<sup>29</sup> has been used to derive the power-law creep related parameters ( $1/\eta_p$  and  $n$ ; Table 1) for two reasons. First, this material was subjected to 65,015 h in service at temperatures between 490°C and 530°C, prior to creep testing.<sup>37</sup> Thus, it is unlikely that GB particle evolution occurs during the test (hence a fixed  $f_b$  value). Second, the operating pressure of less than 20 MPa is low enough to prevent generating creep cavities in this ex-service material, and hence, no need to consider pre-existing cavities in our calculations. Note that the maximum allowable carbon content for Type 316 stainless steel is <0.08 wt.% according to ASME.<sup>38</sup> This means that the chosen material with a carbon content of 0.06 wt.%<sup>39</sup> falls into the category of Type 316 stainless steel.

Figure 2A shows the relationship between  $\sigma_n$  and cavity-growth rate at three different temperatures of 500°C/550°C/600°C, as predicted by Equation 4. The cavity-growth rate increases by 1 order of magnitude with temperature increasing from 500°C to 600°C. However,

the transition value of  $\sigma_n$  ( $\sim 400$  MPa), which differentiates the cavity-growth mechanism under low and high stresses, is not affected by the temperature. This is as expected because the GB diffusion has the same activation energy as the surface diffusion (Table 1). Effects of the radius  $r$  and  $\sigma_n$  on cavity shrinkage rate are shown in a contour plot of Figure 2B, as predicted by Equation 6. Different colors signify temperatures of 500°C/550°C/600°C, respectively. For each temperature, the contour curves with the largest value are always towards the top left, indicating that a higher compressive stress  $\sigma_n$  or smaller cavity radius  $r$  results in a higher shrinkage rate. By comparing different colored curves with the same value, the shrinkage rate is found to be positively correlated with temperature.

## 2.3 | Numerical implementation

Numerical computation of the cavity number density during creep-fatigue was performed in a sectionalized manner. Let us consider a time section  $i$ , the time period starts from  $(i - 1)\Delta t$  and ends at  $i\Delta t$ , and a group of cavities can be nucleated during the time interval  $\Delta t$ . This group of cavities is named as “cavities of the  $i$ th group.” All the cavities belonging to this group would have the same radius, and hence, they are assigned as the nucleated cavities within the time section  $i$ . The number density of cavities of the  $i$ th group is marked as  $\rho_i$ , with its value equaling the product of nucleation rate  $\dot{\rho}_i$  and  $\Delta t$ . The cavity is considered as nucleated when its radius reaches the value of  $2\gamma/\sigma_n$ , and we assign the symbol  ${}^0r_i$  representing the critical nucleation radius.

As the cavity-growth rate changes with size, its value  ${}^j\dot{r}_i$  needs to be recalculated for each group of nucleated

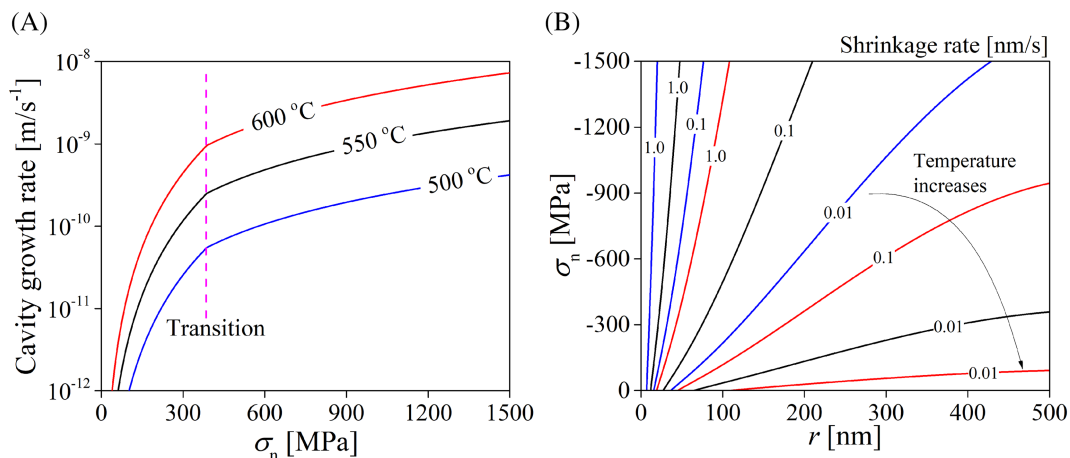


FIGURE 2 Effects of (A) local normal stress  $\sigma_n$  on cavity-growth rate and (B) cavity radius  $r$  and  $\sigma_n$  on shrinkage rate at 500°C (blue), 550°C (black), and 600°C (red) [Colour figure can be viewed at [wileyonlinelibrary.com](https://onlinelibrary.wiley.com)]

cavities at every time sections. For a time section  $k$  ( $k > i$ ), the cavity radius of the  $i$ th group, symbolized as  ${}^{k-i}r_i$ , can be worked out:

$${}^{k-i}r_i = {}^0r_i + \sum_{j=i+1}^k j\dot{r}_i\Delta t, \quad (7)$$

where  ${}^j\dot{r}_i$  is the growth rate at time section  $j$  ( $j > i$ ). This implies that cavities of the  $i$ th group are considered as sintered, when the value of  ${}^{k-i}r_i$  is less than that of  ${}^0r_i$ . Thus, the sintered condition is defined as

$$\sum_{j=i+1}^k j\dot{r}_i\Delta t < 0 \quad (8)$$

A flag variable (e.g.,  $\text{Flag}(i)$  for cavities of the  $i$ th group) is assigned to each cavity group as soon as cavities are nucleated, and this will be updated at following time sections. The flag value of 1 means that this group of cavities still exists, while 0 means that it is as sintered.

The number density of cavities  $\rho(k)$  at the end of time section  $k$  ( $k > i$ ) after taking sintering into account can be formulized as

$$\rho(k) = \rho(k-1) + \rho_k - \sum_{i=1}^{k-1} \left[ \rho_i \left| \sum_{j=i+1}^k j\dot{r}_i\Delta t < 0 \cap \text{Flag}(i) = 1 \right. \right], \quad (9)$$

where  $\rho_k$  is the number density of cavities nucleated within the time section  $k$ . The cavitated GB area fraction  $f(k)$  at the end of time section  $k$  can be then derived with the assumption of idealized hexagonal grain shape:

$$f(k) = \frac{\sqrt{3}}{2} d \times 10^6 \sum_{i=1}^k [\rho_i {}^{k-i}r_i | \text{Flag}(i) = 1]. \quad (10)$$

The coefficient of  $10^6$  has been generated due to the unit conversion that involves the parameters of  $\rho$  in  $\text{mm}^{-2}$ ,  $r$  in  $\mu\text{m}$ , and  $d$  in  $\mu\text{m}$ .

The numerical algorithm is depicted in Figure 3 using a flow chart. First, the material parameters in Table 1 are read by our self-written MATLAB script. Afterwards,  $\Delta t$  is read from input,  $\rho$  and  $\sigma_n$  are set to zero, and the iteration begins at the time section  $k = 1$ . Within each iteration,  $T$  and  $\sigma_s$  at time  $k\Delta t$  are read first; then,  $\sigma_n$  can be calculated by Equation 2. Next, the nucleation rate  $\dot{\rho}$  is computed by Equation 1, from which the initial  $\rho$  that does not consider the sintering effect can be worked out. After this step, the script enters into the sintering module, which is ruled by Equation 9. Note that the flag variable will be updated with a value of 0 if the considered cavity group is found to be as sintered using the criterion given in Equation 8. Afterwards, the cavitated GB area fraction  $f$  can be calculated by Equation 10. At the end of each iteration, time section  $k$  is updated by  $k + 1$ , and a new iteration begins. Refer to Appendix C for the limited numerical error generated by using the forward Euler method together with  $\Delta t = 0.5$  s.

### 3 | MODEL PREDICTION

#### 3.1 | Key outputs

A typical load waveform in stress-controlled creep-fatigue with initial compression under  $\sigma_s \in [-150, 150]$  MPa and  $T = 550^\circ\text{C}$  is shown in Figure 4. The first cycle is presented for illustration purpose, and the following cycles are the same. It consists of

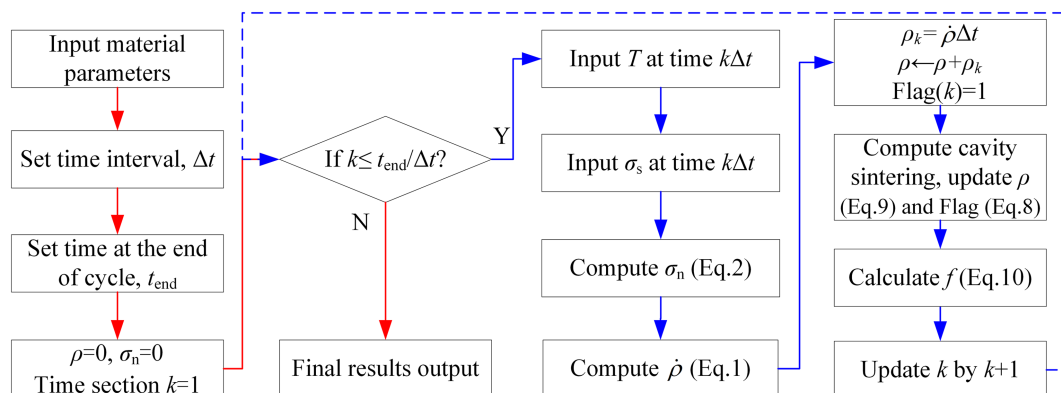


FIGURE 3 Overall flow chart of the numerical computation [Colour figure can be viewed at wileyonlinelibrary.com]

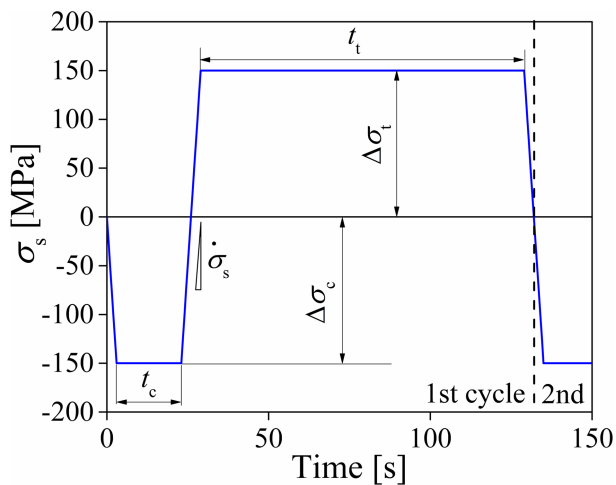


FIGURE 4 A typical stress-controlled creep-fatigue load waveform [Colour figure can be viewed at [wileyonlinelibrary.com](http://wileyonlinelibrary.com)]

a precompressive stress hold for a period  $t_c$  and a tensile stress hold  $t_t$ . The magnitude of stress applied during compression is designated as  $\Delta\sigma_c$ , and the stress applied during tension is  $\Delta\sigma_t$ . The stress variation rate during load reversal is constant, symbolized as  $\dot{\sigma}_s$ . Table 2 summarizes the default value for load-waveform parameters and test temperature. They are used to elaborate the key model outputs. A total number of 50 cycles have been calculated.

Figure 5A shows the model predicted  $\sigma_n$  as a function of the elapsed time/cycle. The maximum  $\sigma_n$  in each cycle is the sum of the relaxed  $\sigma_n$  in precompression and the increment of  $\sigma_n$  induced by the load reversal. The maximum  $\sigma_n$  starts from a value of 761 MPa in the first cycle and then decreases cycle by cycle. After 40 cycles, the maximum  $\sigma_n$  reaches its steady state with a value of 310 MPa, as highlighted by the hatched region in Figure 5A. The evolution of  $\sigma_n$  during the first cycle is shown in Figure 5B, where the magnitude change due to the load reversal from compression to tension appears to be the same as that from tension to compression. In addition, the inset shows that the magnitude of relaxed  $\sigma_n$  in tensile hold (54 MPa) is larger than the compressive hold (11 MPa). This stress difference is caused by the longer tensile hold time  $t_t$  than the compressive time  $t_c$ . Thus, the net  $\sigma_n$  change during the nonsaturation cycle is negative (e.g.,  $-42$  MPa in the first cycle), leading to gradually decreased maximum value of  $\sigma_n$  (Figure 5A).

When cyclic loading continues, the magnitude of relaxed  $\sigma_n$  in tensile hold decreases, whereas that in compressive hold increases. This is as expected because Equation 2 includes an exponential decay function, indicating that an increased initial stress level would cause a faster stress relaxation over a fixed period of time. When the

TABLE 2 Load-waveform parameters and temperature in their default values

Parameters	Default value	Units
$t_c$	20	s
$t_t$	100	s
$\Delta\sigma_c$	150	MPa
$\Delta\sigma_t$	150	MPa
$\dot{\sigma}_s$	50	MPa s <sup>-1</sup>
$T$	550	°C

steady state is reached, the magnitude of relaxed  $\sigma_n$  in the tensile and compressive holds becomes identical. This can be clearly seen in Figure 5C for the 40th cycle, where the tensile and compressive holds introduce a relatively small net stress relaxation of  $-5$  MPa. This means that the net stress change almost reaches the steady state, being consistent with the observation in Figure 5A.

Since nucleation rate is highly sensitive to  $\sigma_n$ , the maximum  $\sigma_n$  is key to cavity nucleation. The model predicted  $\rho$  evolution and cavitated GB fraction  $f$  during 50 cycles of creep-fatigue loading are shown in Figure 5D. The  $\rho$  curve in black shows that most of the cavities are nucleated in the tensile hold of the first cycle, while the following compressive hold contributes to the major part of cavity sintering. After the first two cycles, the change in  $\rho$  becomes negligible. By comparison, the  $f$  curve in red with its value read from the right axis (Figure 5D) shows an overall increasing trend. This implies that the increased  $f$  value in later creep-fatigue cycles is most likely related to the cavity growth rather than the nucleation of new cavities.

To show this more evidently, two enlarged views of the  $f$  curve exhibiting a zigzag shape are highlighted in Figure 5D. The zigzag shape can be explained by the fact that cavities nucleate and grow up when  $\sigma_n > 0$ , while they shrink when  $\sigma_n \leq 0$ . The zigzag characteristic is more noticeable in the second cycle than the 43rd cycle, indicating that the cavity radius change rate reduces with the cycling. This implies that the cavity sintering less likely occurs in the later cycles of creep-fatigue loading under the present waveform condition (i.e.,  $t_t > t_c$  in Figure 4). Since the model predicts that the later creep-fatigue cycles neither nucleate many cavities (black curve in Figure 5D) nor cause the already nucleated cavities to be sintered (red curve in Figure 5D), it is appropriate to reduce fatigue cycles from 50 to 10 to save the computational cost.

In the work by Min and Raj,<sup>18</sup> one purpose-designed creep-fatigue cycle at 625°C was employed to create the increased fatigue crack growth rate from 0.05 to

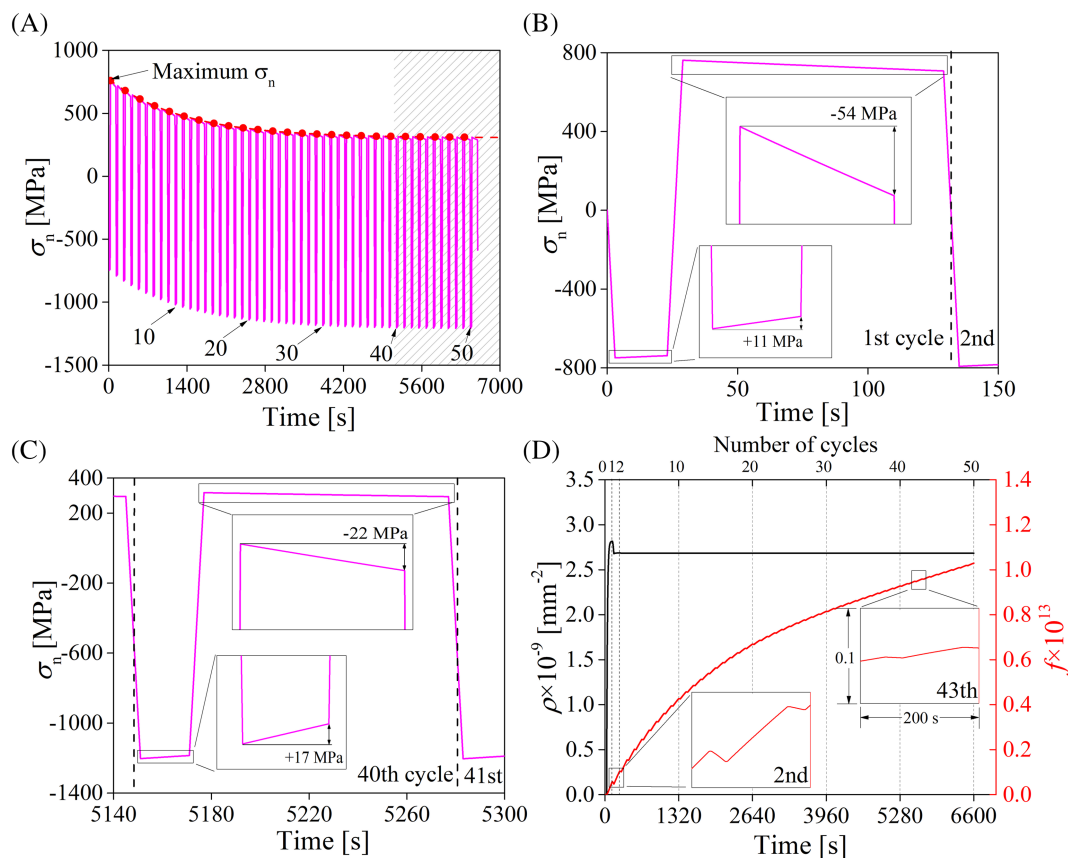


**FIGURE 5** Predicted time-evolution curves of (A) the local normal stress  $\sigma_n$ , (B)  $\sigma_n$  in the first cycle, (C)  $\sigma_n$  in the 40th cycle, and (D) the number density of cavities  $\rho$  and cavitated GB fraction  $f$  [Colour figure can be viewed at [wileyonlinelibrary.com](http://wileyonlinelibrary.com)]

0.17 mm/cycle on the Type 316 stainless steel. This specific load waveform included a 15-min stress hold under compression ( $-382$  MPa), followed by a rapid load reversal from compression to tension (382 MPa) with a strain rate of  $2 \times 10^{-4} \text{ s}^{-1}$  and then applying a 1-h stress hold under tension. The cavitation damage at grain boundaries was responsible for the increased crack growth rate. They also showed that imposing more than one fatigue cycle could not generate a further increase in the crack growth rate. Therefore, our model prediction in terms of the importance of the first fatigue cycle agrees with the experimental observation.

According to the predicted  $\sigma_n$  with a magnitude of 761 MPa (for a tensile hold stress  $\Delta\sigma_t$  of 160 MPa in Figure 5A) in the present work, the cavity nucleation rate would be  $2.1 \times 10^{-10} \text{ mm}^{-2} \text{ s}^{-1}$ . When the magnitude of  $\sigma_n$  increases to 1016 MPa, by applying a higher tensile stress hold of 200 MPa, the nucleation rate increases to  $4.0 \times 10^{-1} \text{ mm}^{-2} \text{ s}^{-1}$ . Recall the work by Raj,<sup>40</sup> the predicted cavity nucleation rate was found to vary from  $10^{14}$  to  $10^{-16} \text{ mm}^{-2} \text{ s}^{-1}$ , if the local normal stress  $\sigma_n$  is decreased by an order of magnitude from  $10^3$  to  $10^2$  MPa. Thus, our model prediction regarding the nucleation rate is as expected. It is well recognized (e.g., Evans<sup>15</sup>) that

cavity nucleation under the GB sliding mechanism would require a high stress concentration (in the order of  $10^3$  to  $10^4$  MPa) particularly associated with the classical nucleation theory. Also, the nucleation rate (and cavity density) is strongly dependent on the material parameters.<sup>19,40</sup>

In this context, it is the predicted trend, rather than the specific value of cavity number density, that provides an important but missing guideline in terms of optimizing the load-waveform design to produce more creep cavitation damage with reduced creep-fatigue experimental cost.

### 3.2 | Effect of loading sequence

Creep-fatigue test can start either with the initial compression or tension. Figure 6A compares these two loading sequences in terms of the  $\sigma_n$  evolution. The load-waveform parameters and temperature used here are the same as that listed in Table 2, that is,  $t_t > t_c$ . It can be seen that the test with initial compression has a higher maximum  $\sigma_n$  than that with initial tension. This is because the precompression period can relax the  $\sigma_n$ ,

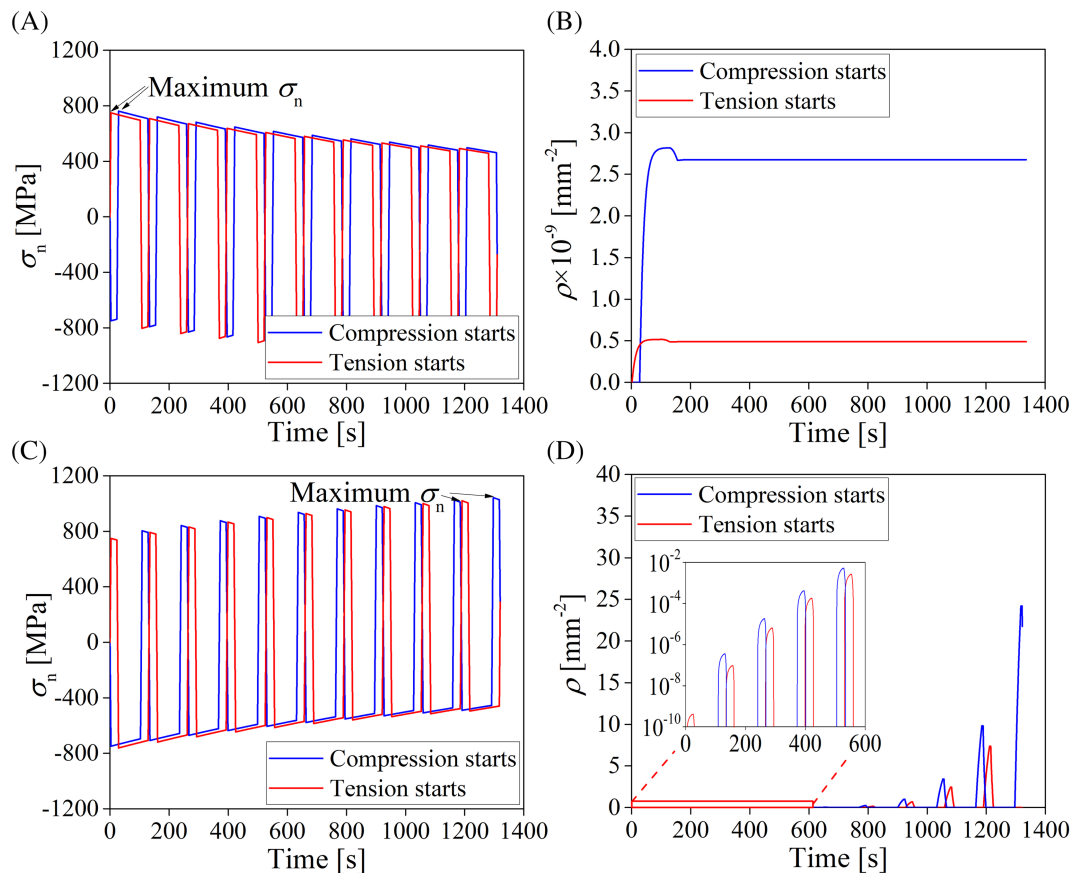


**FIGURE 6** Creep-fatigue test with initial compression is compared with initial tension: (A,B) The time evolution of  $\sigma_n$  and  $\rho$  for the test condition of  $t_t = 100$  s,  $t_c = 20$  s (i.e.,  $t_t > t_c$ ) and (C,D) the time evolution of  $\sigma_n$  and  $\rho$  for the test condition of  $t_t = 20$  s,  $t_c = 100$  s (i.e.,  $t_t < t_c$ ) [Colour figure can be viewed at [wileyonlinelibrary.com](http://wileyonlinelibrary.com)]

contributing to the higher maximum  $\sigma_n$  in the tension phase. The difference of maximum  $\sigma_n$  between the two loading conditions is 12 MPa, which is in line with the relatively short  $t_c$  of 20 s. The number density of cavities  $\rho$  after 10 cycles was calculated as  $2.6 \times 10^{-9} \text{ mm}^{-2}$  for the test with initial compression, which is approximately 1 order of magnitude higher than that with initial tension ( $\rho = 4.9 \times 10^{-10} \text{ mm}^{-2}$ ), Figure 6B.

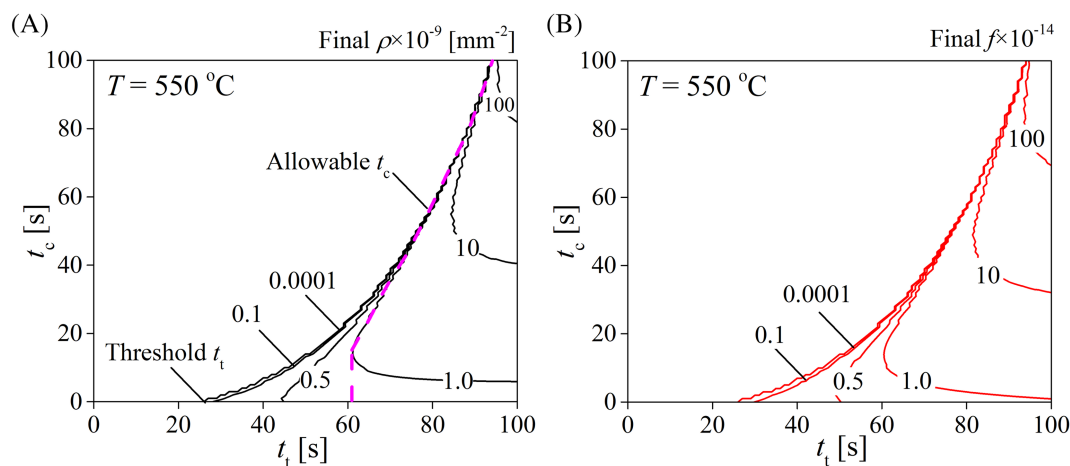
Now, let us consider a completely different scenario in which the compressive hold is prolonged, that is,  $t_c > t_t$ . To this end, the  $\sigma_n$  evolution for a creep-fatigue loading with  $t_t = 20$  s and  $t_c = 100$  s was calculated. The test with initial compression is compared with that with initial tension. For both cases, the  $\sigma_n$  increases cycle by cycle, and the maximum  $\sigma_n$  appears at the last cycle (Figure 6C). The test with initial compression has a higher maximum  $\sigma_n$  than that with initial tension. At the first cycle, the stress difference is 54 MPa, reducing to 23 MPa at the 10th cycle (the last cycle of calculation). This implies that the maximum  $\sigma_n$  difference between the two loading conditions will eventually diminish to 0 MPa if the cyclic loading continues.

Figure 6D depicts the time evolution of  $\rho$  curves for these two test conditions. After each cycle, the  $\rho$  curves drop to 0, indicating that all of the cavities nucleated in the tension phase are sintered during the subsequent long compressive hold ( $t_c = 100$  s). By comparison of Figure 6B with Figure 6D, it can be known that the nucleation rate in the tests with  $t_c = 100$  s is almost 10 orders of magnitude higher than that in the tests with  $t_c = 20$  s. This is because the maximum  $\sigma_n$  is higher in the test with  $t_c = 100$  s (1043 MPa in Figure 6A) when compared with that test with  $t_c = 20$  s (761 MPa in Figure 6C). However, this does not necessarily lead to the overall increase of cavitation damage as the prolonged compressive hold would also cause sintering and close all cavities nucleated in the previous tension phase.

### 3.3 | Combined effect of tensile and compressive holds

Combined effect of  $t_t$  and  $t_c$  on the final  $\rho$  after 10 cycles is presented in Figure 7A by the contour plot. Note that





**FIGURE 7** Dependences of the cavity number density  $\rho$  after 10 cycles in (A) and the cavitated GB area fraction  $f$  in (B) on the tensile and compressive hold times of  $t_t$  and  $t_c$  [Colour figure can be viewed at [wileyonlinelibrary.com](https://onlinelibrary.wiley.com)]

except for the  $t_t$  and  $t_c$ , the default value as given in Table 2 is used for all the other load-waveform parameters and temperature. The contour curves of 0.1 and 0.0001 in Figure 7A are very close to each other, suggesting that the contour curve of 0.1 can be used as the lower bound value. In other words, below this value, the final  $\rho$  is negligible. There is a threshold value of  $t_t$  for cavitation when  $t_c = 0$  s, indicating that the nucleated cavities can be sintered by the load reversal from tension to compression. In addition, under the condition of  $t_c = 0$  s, the contour curves with values of 0.5 and beyond do not intercept the  $x$  axis. This indicates that there is an upper bound value for  $t_t$ ; any prolonged tensile hold  $t_t$  than this critical value would not further contribute to the final  $\rho$ . This is probably attributed to the rapid decrease of  $\sigma_n$  during tensile hold as informed by the exponential decay function in Equation 2.

Now, let us focus on the changing values of  $t_c$ . When  $t_t$  is less than 60 s, increasing  $t_c$  helps to reduce the final  $\rho$ . But when  $t_t$  is greater than 60 s, an increased  $t_c$  promotes the increased final  $\rho$  until reaching the allowable value as highlighted by the magenta dash curve in Figure 7A. It is also evident that the allowable  $t_c$  increases with the increasing  $t_t$ . The presence of allowable  $t_c$  is the result of two competing effects: (i) The increased  $t_c$  can promote the cavity nucleation rate by affecting the maximum  $\sigma_n$  in the next tension phase; (ii) the prolonged  $t_c$  increases the likelihood of cavity sintering process, given the compressive stress.

Furthermore, the combined effect of  $t_t$  and  $t_c$  on the final  $f$  is presented in Figure 7B. The distribution of contour curves looks similar by comparing Figure 7A with Figure 7B, suggesting that the dependence of final  $\rho$  and  $f$  on the load-waveform parameters are highly consistent,

that is, both are positively correlated with the maximum  $\sigma_n$ .

### 3.4 | Effect of stress magnitude in tensile and compressive holds

Figure 8A presents the effect of  $\Delta\sigma_t$  on final  $\rho$  (i.e., calculated after 10 cycles); the values of  $\Delta\sigma_t$  and  $t_t$  are varied for this purpose. Other input parameters are kept the same (Table 2). A positive correlation is found between  $\rho$  and  $\Delta\sigma_t$  for both  $t_t = 100$  and 60 s, suggesting that a higher tensile stress promotes a higher cavity nucleation rate. However, the breakdown of this correlation occurs when  $\Delta\sigma_t$  is lower than  $\sim 145$  MPa under the condition of  $t_t = 60$  s. This sharp decrease in final  $\rho$  is related to the effect of compression phase on cavity sintering. When the tensile stress reduces to lower level, the associated  $\sigma_n$  under a fixed  $t_t$  does not allow the nucleated cavities to grow large enough to be survived from the following compression phase where sintering occurs. As shown in the enlarged view of Figure 8A, such a threshold  $\Delta\sigma_t$  appears at the level of  $\sim 105$  MPa under the condition of  $t_t = 100$  s. This means that the threshold value for  $\Delta\sigma_t$  to generate the cavitation is inversely proportional to  $t_t$  (i.e., 145 MPa for  $t_t = 60$  s while 105 MPa for  $t_t = 100$  s).

In terms of the effect of  $\Delta\sigma_c$  on the final  $\rho$ , a positive correlation is found between the two until  $\Delta\sigma_c$  reaching the breakdown value (Figure 8B). Such breakdown of the positive correlation can be seen when  $\Delta\sigma_c > 120$  MPa under the condition of  $t_t = 60$  s. This is followed by a sharp drop of final  $\rho$  when  $\Delta\sigma_c > 160$  MPa. With the increase of tensile hold time to  $t_t = 100$  s, the breakdown

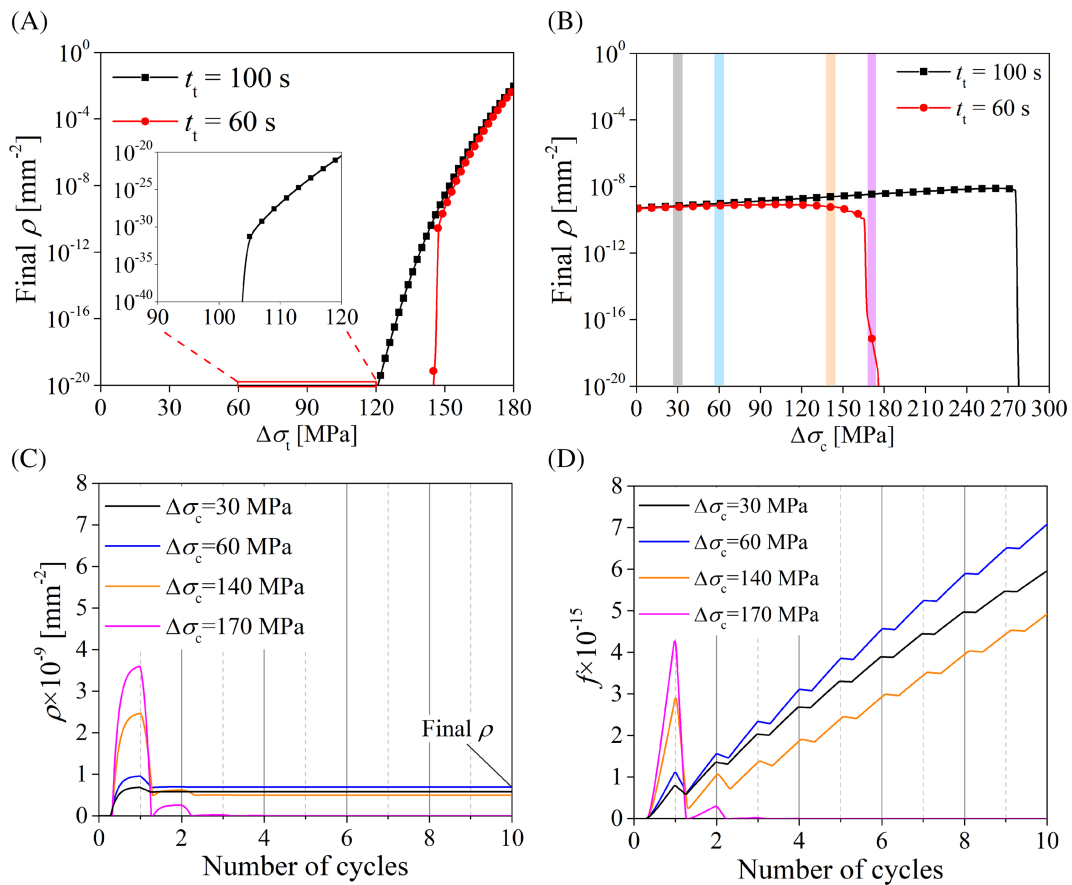


**FIGURE 8** The dependence of final  $\rho$  on (A)  $\Delta\sigma_t$  and (B)  $\Delta\sigma_c$  with  $t_t = 60/100$  s; the evolution of  $\rho$  in (C) and  $f$  in (D) as a function of fatigue cycles calculated with different stress magnitudes of  $\Delta\sigma_c = 30/60/140/170$  MPa but under the same tensile hold time of  $t_t = 60$  s [Colour figure can be viewed at [wileyonlinelibrary.com](http://wileyonlinelibrary.com)]

occurs at a higher compressive stress of when  $\Delta\sigma_c > 270$  MPa.

To explain this interesting phenomenon, the change of  $\rho$  and  $f$  as a function of cycles are presented in Figure 8C,D, respectively. Four different stress levels of  $\Delta\sigma_c = 30/60/140/170$  MPa are considered, and they represent different characteristic regions as highlighted by using different colors in Figure 8B. Comparing the values of  $\rho$  at the end of the first cycle, the test with  $\Delta\sigma_c = 170$  MPa has the largest  $\rho$  of  $3.6 \times 10^{-9}$  mm<sup>-2</sup>, whereas that with  $\Delta\sigma_c = 30$  MPa shows the smallest  $\rho$  of  $0.7 \times 10^{-9}$  mm<sup>-2</sup> (Figure 8C). This indicates that a higher  $\Delta\sigma_c$  helps to produce more creep cavities in the subsequent tension phase. However, in the next compression phase of the second cycle, these nucleated cavities would be sintered to different extents depending on the stress level of  $\Delta\sigma_c$ . For example, the  $\rho$  value reduction is found to be  $-0.2 \times 10^{-9}$ ,  $-0.3 \times 10^{-9}$ ,  $-1.9 \times 10^{-9}$ , and  $-3.6 \times 10^{-9}$  mm<sup>-2</sup> for  $\Delta\sigma_c = 30, 60, 140,$  and  $170$  MPa, respectively, (Figure 8C). Thus, the competing effect of  $\Delta\sigma_c$  on  $\rho$  through the cavity nucleation and sintering leads to the fact that an intermediate level of  $\Delta\sigma_c$  is more likely to create more cavities.

For the same reason, the breakdown of the positive correlation between the final  $\rho$  and  $\Delta\sigma_c$  as revealed in Figure 8B can be explained by the sintering effect that becomes predominant when the compressive stress is sufficiently large. In terms of the cavitated GB fraction  $f$ , its value increases with the number of cycles (Figure 8D). The zigzag shape in the  $f$  curves reflects the alternating nucleation and sintering events. In summary, increasing the stress level of  $\Delta\sigma_t$  is more effective in enhancing the final  $\rho$  when compared to  $\Delta\sigma_c$ . The underlying mechanism is the side effect associated with the cavity sintering due to the increased  $\Delta\sigma_c$ .

### 3.5 | Effect of stress variation rate

After elaborating the effects of four input parameters ( $t_t$ ,  $t_c$ ,  $\Delta\sigma_t$ , and  $\Delta\sigma_c$ ), we now consider the effect of stress variation rate  $\dot{\sigma}_s$  (Figure 4). To limit the effect of hold time on the prediction results, both  $t_c$  and  $t_t$  are set to 0 s for calculations. Figure 9A shows the effect of  $\dot{\sigma}_s$  on the final  $\rho$  and  $f$  after 10 cycles. There is an optimum value of  $\dot{\sigma}_s$  ( $\sim 0.4$  MPa s<sup>-1</sup>) that leads to the maximum final  $\rho$  and  $f$ .

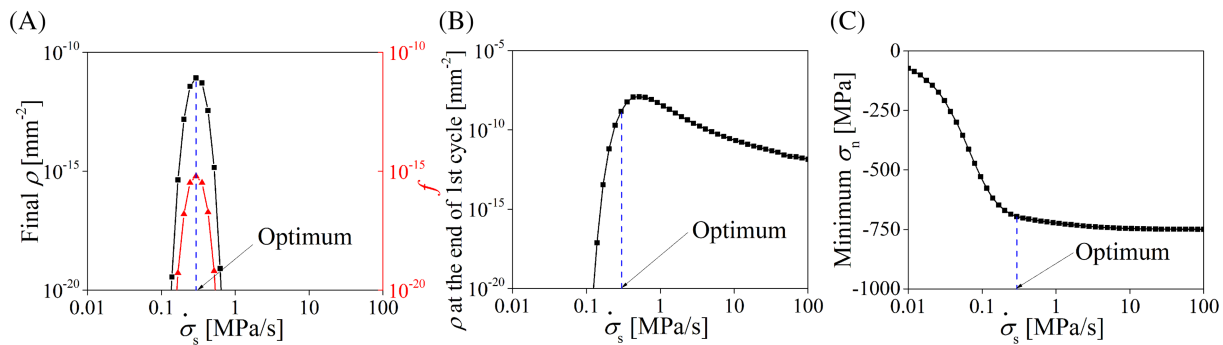


**FIGURE 9** (A) Dependence of final  $\rho$  and  $f$  on stress variation rate  $\dot{\sigma}_s$  under  $t_c$  and  $t_t = 0$  s, (B)  $\rho$  value at the end of first cycle, and (C) the related minimum  $\sigma_n$  in the compression phase of second cycle [Colour figure can be viewed at [wileyonlinelibrary.com](https://onlinelibrary.wiley.com/doi/10.1111/ffe.13643)]

To explain its presence, the  $\rho$  values as calculated at the end of first cycle (i.e., the moment of finishing the tension phase) are presented in Figure 9B, while the minimum  $\sigma_n$  as calculated in the second cycle (i.e., the following compression phase) are shown in Figure 9C. Note that the magnitude of  $\rho$  at the end of first cycle can be regarded as the evaluation of the nucleation ability in the considered load-waveform shape. Equally, the absolute value of the minimum  $\sigma_n$  in the second cycle can be regarded as the evaluation of the sintering ability.

Figure 9B shows that  $\rho$  decreases rapidly with the decrease of  $\dot{\sigma}_s$  in the range of  $\dot{\sigma}_s < 0.4 \text{ MPa s}^{-1}$ . This implies that a too low stress variation rate reduces the nucleation ability. This seems to agree with the previous one-cycle creep-fatigue modeling work,<sup>19</sup> where the local normal stress relaxation was found to occur during the load reversal with low  $\dot{\sigma}_s$ . On the other hand, the  $\rho$  curve decreases with the increase of  $\dot{\sigma}_s$  when  $\dot{\sigma}_s > 0.4 \text{ MPa s}^{-1}$ . At first glance, this might be attributed to the lack of nucleation time when  $\dot{\sigma}_s$  becomes sufficiently high. However, a closer examination of the change of final  $\rho$  in Figure 9A in comparison with the  $\rho$  curve in Figure 9B does not support the above explanation. It is evident that the final  $\rho$  quickly decreases to a value of  $10^{-20} \text{ mm}^{-2}$  with increased  $\dot{\sigma}_s$  (Figure 9A), whereas the  $\rho$  at the end of first cycle decreases moderately to  $10^{-12} \text{ mm}^{-2}$  (Figure 9B).

It is thus hypothesized that the enhanced cavity sintering effect contributed to the rapid decrease in the high  $\dot{\sigma}_s$  range. Figure 9C shows that the absolute value of the minimum  $\sigma_n$  has a monotonically increasing trend with the increase of  $\dot{\sigma}_s$ . This suggests that the sintering effect becomes more pronounced in the high  $\dot{\sigma}_s$  range, causing the final  $\rho$  to decrease, as revealed in Figure 9A. To this end, our hypothesis is verified by the observation.

Finally, it can be seen in Figure 9B that the optimum  $\dot{\sigma}_s$  does not coincide with the value of  $\dot{\sigma}_s$  producing the maximum  $\rho$  value. It is the combined effect of sintering and nucleation over the course of 10 cycles that

determines the optimum  $\dot{\sigma}_s$  value leading to the highest final  $\rho$  in Figure 9A (for brevity not shown here).

## 4 | MODEL APPLICATIONS

### 4.1 | Nucleation incubation time

An incubation time is required to nucleate cavities.<sup>5</sup> The underlying mechanism is the time consumed for vacancies gathering into the nuclei to form a stable cavity.<sup>40</sup> In our model predictions, there is a threshold value of  $t_t$  for creep-fatigue tests without applying compressive stress hold ( $t_c = 0$  s) (Figure 7A). This can be considered as the equivalent nucleation incubation time. Figure 10 presents the calculated values for Type 316 stainless steel under compressive/tensile stresses of (in MPa):  $-150/+150$ ,  $-100/+150$ , and  $-150/+100$  at different temperatures. The increase of temperature by  $50^\circ\text{C}$  reduces the incubation time more than one half.\* This agrees with the experimental data trend on dispersion-strengthened copper alloy between  $700^\circ\text{C}$  and  $800^\circ\text{C}$ .<sup>41</sup> If we take the prediction curve of  $-150/+150$  MPa as the comparison reference, decreasing the tensile stress by 50 MPa results in doubling the incubation time (Figure 10). On the other hand, the incubation time is shortened by 25%, when the compressive stress is decreased by 50 MPa.

Overall, our cavitation model informs that temperature and tensile stress are two influencing factors for the nucleation incubation time. For comparison purposes, experimental results are plotted as red data points in Figure 10. The “no cavity” data were obtained from the work by Shi and Pluvinaige.<sup>42</sup> The creep-fatigue test was conducted at  $500^\circ\text{C}$  on Type 316L stainless steel under total strain range of 1.60% (stress amplitude of 350 MPa)

\*It is understood that this observation applies to the temperature level of 0.4 times the melting temperature ( $500^\circ\text{C}$  and above) of Type 316 stainless steel, but it may not be accurate at lower temperatures.

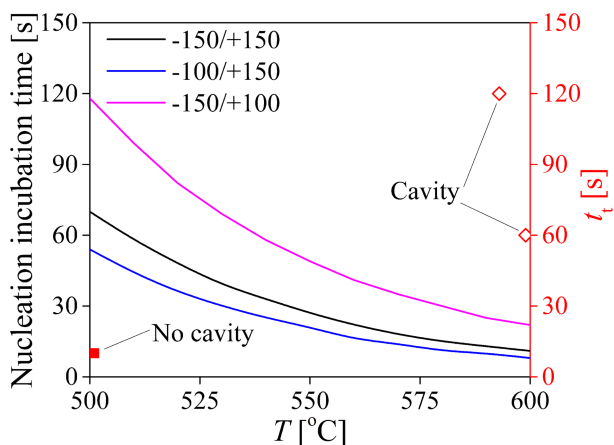


**FIGURE 10** Model predicted nucleation incubation time (with stress amplitude and temperature indicated) in comparison with experimental data. Experimental data points are collected from creep–fatigue tests on Type 316 stainless steel [Colour figure can be viewed at [wileyonlinelibrary.com](#)]

together with tensile hold of  $t_t = 10$  s. They observed no creep cavitation damage, being consistent with the transgranular crack propagation mode. In addition, the 600°C “cavity” data point was obtained from the creep–fatigue test on Type 316 stainless steel conducted by Hales.<sup>1</sup> Cavitation damage was found under the test condition of total strain range of 0.5% and  $t_t = 60$  s. No stress–strain hysteresis loop was given, and hence, the stress amplitude has been calculated as 140 MPa using relevant database in ASME.<sup>38</sup> The 593°C “cavity” data point was obtained from the creep–fatigue crack growth test on Type 316 stainless steel conducted by Michel and Smith.<sup>43</sup> The test was performed with the initial stress intensity factor range of  $20 \text{ MPa m}^{-2}$ , and they observed intergranular creep damage. In summary, our model prediction agrees with the experimental observation.

## 4.2 | Cycle frequency range

Cavitation can also appear in high-temperature fatigue tests under certain range of cycle frequencies.<sup>44</sup> The cycle frequency that is positively correlated with the stress variation rate can be defined as  $2\dot{\sigma}_s/(\Delta\sigma_c + \Delta\sigma_t)$ . The optimum  $\dot{\sigma}_s$  for final  $\rho$  calculated under the condition of without stress hold (i.e.,  $t_c$  and  $t_t = 0$  s) has been indicated in Figure 9A. This allows us to examine the nucleation ability under different cycle frequency range for high-temperature fatigue.

The frequency range for cavity nucleation depends on both the temperature and stress amplitude. Figure 11 presents the predicted nucleation field in the stress amplitude and frequency space at 550°C and 600°C. Here, the

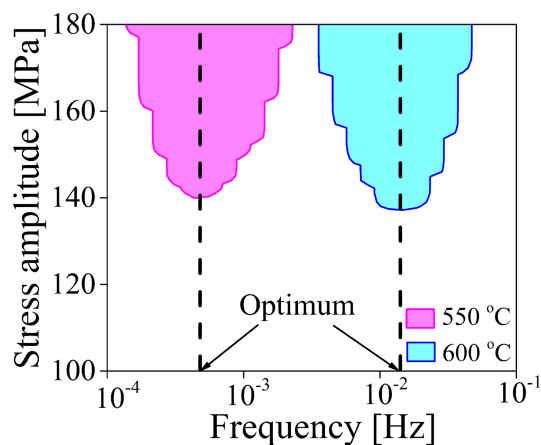


**FIGURE 11** Model predicted cavity nucleation field in stress amplitude and frequency space for Type 316 stainless steel at 550°C and 600°C [Colour figure can be viewed at [wileyonlinelibrary.com](#)]

nucleation criterion is defined as the final  $\rho$  of  $\geq 10^{-20} \text{ mm}^{-2}$ . In other words, if the condition of  $\rho < 10^{-20} \text{ mm}^{-2}$  is met, the combination of stress amplitude and frequency is judged as being unable to create cavitation. The shape of the nucleation field looks like the upside-down hills. This means that the load waveform with a higher stress amplitude has a wider range of cycle frequencies to promote cavitation. Also, an optimum frequency is found at each temperature, allowing the lowest stress amplitude to meet the cavitation criterion. The presence of optimum frequency shares the same mechanism as the optimum  $\dot{\sigma}_s$  in Figure 9. At low frequency, the lack of nucleation ability is the reason, whereas enhanced sintering is responsible for the reduced cavities at high frequency.

It is also interesting to note that the optimum frequency and the whole frequency range are positively correlated with temperature (Figure 11). This can be explained by the time constant  $\tau$  (Equation 3).  $\tau$  is inversely proportional to temperature, given that  $k_e$  is temperature independent, but both the  $\eta_b$  and  $\eta'_p$  are inversely proportional to temperature. As commented in the work,<sup>18</sup> a lower  $\tau$  means that a higher stress variation rate would be required to achieve the same level of  $\sigma_n$  leading to cavitation. Therefore, the nucleation frequency increases with the temperature (i.e., decreasing  $\tau$ ).

Taplin et al.<sup>45</sup> and Tang et al.<sup>46</sup> developed a mechanism map for cavity nucleation in the stress amplitude and frequency space. For GB sliding-induced cavitation, their predicted nucleation frequency for Type 304 stainless steel was in the range from  $3 \times 10^{-2}$  to 1 Hz under stress amplitude of 180 MPa and  $3 \times 10^{-2}$  to  $5 \times 10^{-1}$  Hz under stress amplitude of 140 MPa, respectively. This agrees with our model prediction in a sense that a higher stress amplitude leads to a wider range of nucleation

frequencies. Also, the frequency ranges obtained at 650°C in their predictions are generally higher than our model predictions at 600°C ( $3 \times 10^{-3}$  to  $5 \times 10^{-2}$  Hz) (Figure 11). Thus, our model prediction successfully captures the positive correlation between the nucleation cycle frequency and temperature.

### 4.3 | Unequal ramp rate

High-temperature fatigue testing with unequal ramp rate is an alternative method to study cavitation damage during creep-fatigue interaction.<sup>5</sup> Yamaguchi and Kanazawa<sup>47</sup> studied effects of unequal ramp rate on the strain-controlled high-temperature fatigue in Type 316 stainless steel at 600°C. It was found that the test with a slow-fast cycling waveform exhibited an intergranular fracture mode, and the fatigue life was reduced significantly due to creep cavitation. By comparison, the test with a fast-slow waveform fractured in a transgranular manner, with limited fatigue life reduction.

Now, let us consider the unequal ramp rate scenarios from the modeling perspective. Figure 12A presents the time-evolution curves of  $\sigma_s$  for both the fast-slow and slow-fast cycling, and they were used as the model input. The corresponding  $\rho$  curves in black are shown in Figure 12B. It can be seen that the  $\rho$  in fast-slow test gradually increases after a few cycles, whereas that of the slow-fast test accumulates negligible number of cavities. This is in conflict with the experimental results as the failure of slow-fast test was dominated by creep cavitation. To reconcile this seemingly contradictory phenomenon, it is important to recollect the concept of our cavity nucleation and early-stage growth model.

Schematic diagram in Figure 13 depicts the whole process of creep cavitation. The respective nucleation and subsequent early-stage growth in Figure 13A,B are the main focus of the present work. Since the nucleated cavities are extremely small ( $<0.1 \mu\text{m}$ ) compared with the particles at GB, they are surrounded by a highly localized and time-dependent stress field  $\sigma_n$ , induced by the GB sliding with the rate of  $\dot{U}_{sb}$  (Figure 13B). However, the growth mechanism of large-sized cavities would be completely different. Figure 13C shows that the large cavity is surrounded by a uniform stress field under the far-field stress  $\sigma_s$ . The cavity coalescence shown in Figure 13D is also affected by the stress concentration, but this stress concentration is due to the reduction in effective load-bearing area,<sup>48</sup> which approximately equals  $\sigma_s/(1-f)$  according to Cocks and Ashby.<sup>49</sup> Therefore, it can be considered that the local normal stress  $\sigma_n$  is key to early-stage creep cavitation, whereas the far-field stress  $\sigma_s$  controls its late stage.

In the late-stage cavitation, damage increase is manifested by the radius increase of large cavities. According to the traditional growth model, the growth rate is positively correlated with the cavity radius.<sup>24,50,51</sup> Also, the late-stage growth rate is controlled by applied stress  $\sigma_s$ . Therefore, the time integral of  $\sigma_s$  can be used to assess the propensity of late-stage growth under a given load-waveform shape. In this sense, a positive value of the integral of  $\sigma_s$  indicates that the cavities would continue growing up, whereas a negative value indicating shrinkage in size. Bearing the difference between the early stage and late stage in mind, the  $\rho$  curves in Figure 12B for the fast-slow and slow-fast can be reconciled as below.

The time integral of  $\sigma_s$  (red curves) for the two scenarios are superimposed in Figure 12B with their values

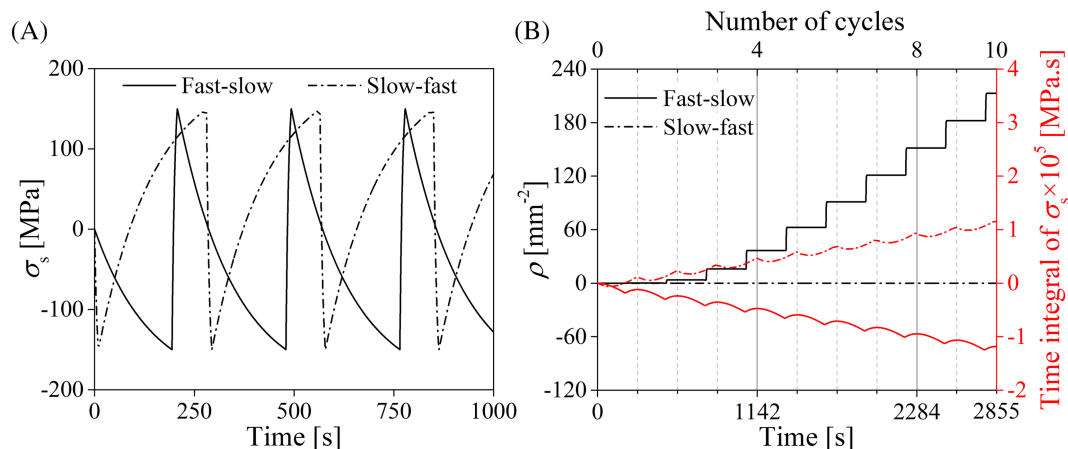


**FIGURE 12** (A) Applied stress as a function of time for the fast-slow and slow-fast creep-fatigue load waveforms and (B) predicted time evolution of  $\rho$  and the time integral of  $\sigma_s$  at 600°C [Colour figure can be viewed at [wileyonlinelibrary.com](http://wileyonlinelibrary.com)]



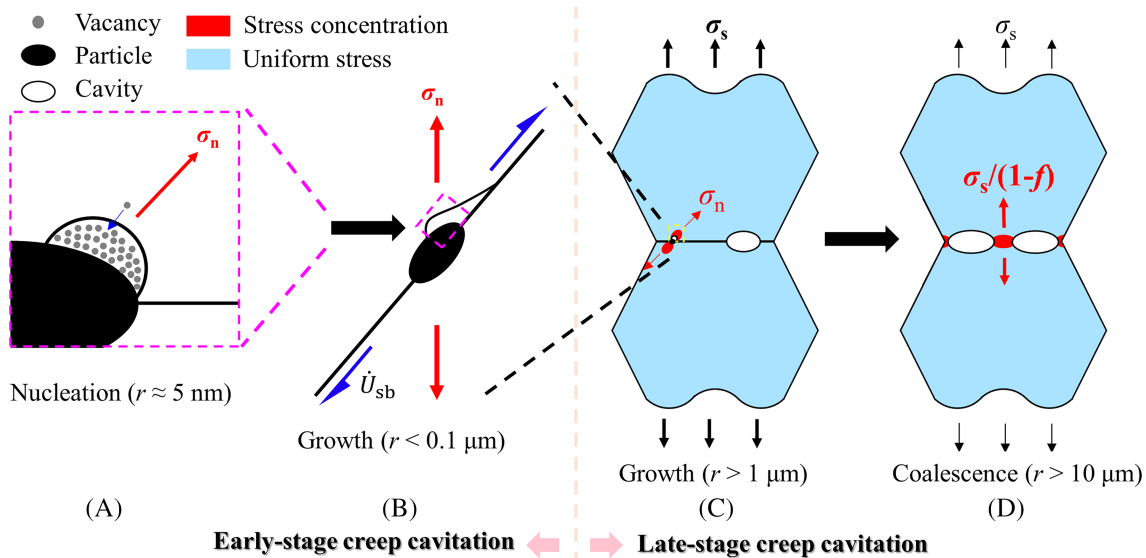


**FIGURE 13** A schematic diagram of cavitation with particular emphasis on the difference between early- and late-stage cavity growth: (A) nucleation, (B) early stage, (C) late stage, and (D) coalescence [Colour figure can be viewed at wileyonlinelibrary.com]

indicated by the secondary  $y$  axis. The slow-fast one shows a positive value of the  $\sigma_s$  integral, whereas the fast-slow one shows a negative value. This implies that cavities in the case of fast-slow are difficult to grow under the negative value of  $\sigma_s$  integral. By contrast, cavities formed in the slow-fast cycling are more likely to grow, although their number density is much less compared to that in the fast-slow one. This eventually leads to an increased cavitated GB fraction  $f$  in the slow-fast. The cavity coalescence occurs when  $f$  becomes sufficiently large, causing the formation of intergranular cracks in macroscopic scale. Hence, cavitation associated intergranular fracture most likely occurs in the slow-fast instead of the fast-slow, as experimentally observed in Rodriguez and Rao<sup>5</sup> and Yamaguchi and Kanazawa.<sup>47</sup>

Although the term *stress* (local normal stress vs. far-field stress) is considered here as the driver for controlling the cavity nucleation, early-stage, and late-stage growth behaviors, one should note that a further consideration from the *strain energy* (locally stored strain energy vs. far-field stress) perspective is a worthwhile effort. In a study of fatigue crack growth behavior, Wilson et al.<sup>52,53</sup> found that the grain-level fatigue crack growth path and the small variation of the growth rate were affected by the locally stored strain energy. By contrast, the primary crack growth rate was influenced by the crack length and the far-field stress applied. Further reading on the microstructurally small fatigue crack is recommended, and a recently published review paper by Jirandehi and Khonsari<sup>54</sup> provides a comprehensive list of references.

#### 4.4 | Cavity early-growth and shrinkage models

There are totally six equations in Section 2.1. Equations 1 to 3 are based on the classical nucleation theories. Equation 1 was taken directly from the nucleation model in the work by Raj and Ashby.<sup>55</sup> Equation 2 is a modified version when compared to its original form given in the work,<sup>18</sup> with the difference being the addition of creep term ( $\eta'_p$ ) to consider the effect of creep deformation compatibility in the neighboring grains. The direct derivation of this new term can be found in Appendix A. Using this modified model in conjunction with Equation 1, a linear relation between the number density of cavities and creep strain can be obtained, and such a relationship has been observed in a creep experiment on Type 347 stainless steel by Needham and Gladman.<sup>56</sup> Equation 3 provides the derivation of time constant ( $\tau$ ) used in Equation 2. This term generates a saturation effect of creep hold time on fatigue life reduction, with its value being negatively correlated to temperature. Experimentally, it has been frequently observed that with the temperature decrease, a longer hold time would be required to obtain the condition that any further increase would cause little change in fatigue life in creep-fatigue tests performed on Type 316 stainless steel.<sup>47,57</sup>

Equations 4 and 5, taken from the cavity-growth model by Nix et al.,<sup>34</sup> are used here to provide the prediction of cavity growth, while Equation 6, taken from the cavity-growth model by Riedel,<sup>35</sup> is used here to predict the shrinkage. Due to the lack of in situ experimental observation of cavity nucleation, growth, and shrinkage

processes especially for the cavity size of below 0.1  $\mu\text{m}$ , defined as the early-stage cavitation here, we could only perform a theoretical verification by comparing the present modeling observations with those based on the other alternative cavity-growth models. In total, six types of cavity-growth mechanisms have been proposed in the past decades,<sup>3</sup> including

1. GB diffusion,
2. surface diffusion,
3. GB sliding,
4. constrained diffusional process,
5. plasticity, and
6. coupled diffusional and plastic growth.

Equations 4 and 5 were developed based on Mechanism 2, while Equation 6 was based on Mechanism 1. Both Mechanisms 1 and 2 are based on diffusion theories. To transport a vacancy from its source to form a cavity, both the GB and surface diffusion processes are involved.<sup>22</sup> Generally, GB diffusion coefficient is the rate-limiting factor (i.e.,  $D_B < D_S^3$ ) of this cascaded process. This means that the cavity shape is not changed during the growth (i.e., equilibrium condition). To this end, all the latest cavity-growth models accept that GB diffusion process is predominant. This seems to be true for cavities of 0.1  $\mu\text{m}$  or larger in radius according to experimental verification by Kumar et al.<sup>58</sup> However, whether it holds true for a cavity of far smaller than 0.1  $\mu\text{m}$  is unknown. Chen<sup>25</sup> pointed out that GB sliding played an important role in the early-stage cavity growth, and the cavity tip velocity during the GB sliding process was limited by surface diffusion. This implies that Mechanism 3 can be regarded as a variant of Mechanism 2. Similarly, the growth models based on Mechanism 4 can be regarded as a variant of Mechanism 5 as the former states that the growth rate is controlled by plastic deformation rate. Note that the plasticity controlled growth mechanism is frequently used under the condition of high-strain rate and large cavity size.<sup>3</sup>

To summarize, there are two primary mechanisms responsible for the cavity-growth processes: diffusion and plasticity. A unified cavity-growth model was firstly proposed by Beere and Speight<sup>59</sup> to consider both the GB diffusion and plasticity, that is, Mechanism 6. Such a model was further developed by Needleman and Rice,<sup>22</sup> who introduced a concept of diffusion length that defines only if cavity radius exceeds it can plasticity controlled cavity-growth mechanism becomes important:

$$\Lambda = \left( \frac{\delta D_B \Omega \sigma_s}{kT \dot{\epsilon}} \right)^{1/3} = \left( \frac{\delta D_B \Omega \eta_p}{kT \sigma_s^{n-1}} \right)^{1/3}, \quad (11)$$

where  $\sigma_s$  is far-field applied stress and  $\dot{\epsilon}$  is the creep rate. The power-law creep can link the two by  $(1/\eta_p) \sigma_s^n$ . This coupled cavity-growth model and its variants have been used in the rupture prediction under creep<sup>51,60</sup> and creep-fatigue,<sup>9</sup> with the most widely used version proposed by Sham and Needleman<sup>61</sup>:

$$\dot{r} = \dot{r}_{df} + \dot{r}_{cr}, \quad (12)$$

$$\frac{\dot{r}_{df}}{\dot{\epsilon} r} = \left( \frac{\Lambda}{r} \right)^3 \left[ \frac{1 - (1-f) \frac{2r}{r} / \sigma_s}{\ln(1/f) - (3-f)(1-f)/2} \right], \quad (13)$$

$$f = \max \left[ \left( \frac{r}{b} \right)^2, \left( \frac{r}{r+1.5\Lambda} \right)^2 \right], \quad (14)$$

$$\frac{\dot{r}_{cr}}{\dot{\epsilon} r} = \frac{1}{2} \left[ 1 + (n-1)(n+0.4319)/n^2 \right]^n, \quad (15)$$

where  $\dot{r}_{df}$  represents the cavity radius growth rate contributed by diffusion and  $\dot{r}_{cr}$  represents that contributed by plasticity (i.e., creep rate).

Here, a comparative study is performed to assess the similarity and discrepancy between the newly proposed early-stage growth model and the traditional late-stage growth model (e.g., Sham and Needleman<sup>61</sup>). All the calculations have been made under the following conditions: temperature of 500°C, far-field stress  $\sigma_s$  of 50 and 200 MPa, and local normal stress  $\sigma_n$  with the value of  $\sigma_s/f_b$  (approximating to the maximum value of  $\sigma_n$  under cyclic loading with the waveform parameters given in Table 2). The material parameters used in the calculations can be found in Table 1.

Figure 14A,B compares the cavity-growth rates calculated by using the Sham and Needleman model with those calculated using the present early-stage growth model, under two different far-field stress levels. Our proposed model predicts a constant growth rate, being independent on the cavity radius (red solid line), whereas the Sham and Needleman model gives a growth rate that is dependent on the radius (black solid line). The respective contribution of the diffusion versus plasticity term to the cavity growth as predicted by the Sham and Needleman model is illustrated in Figure 14 by using blue dashed line with circles and magenta dashed line with squares. By increasing the far-field stress level from 50 (Figure 14A) to 200 MPa (Figure 14B), it is evident that the cavity-growth controlling mechanism switches from diffusion to plasticity. The growth rate predicted by our model using  $\sigma_n$  is higher than GB diffusion controlled

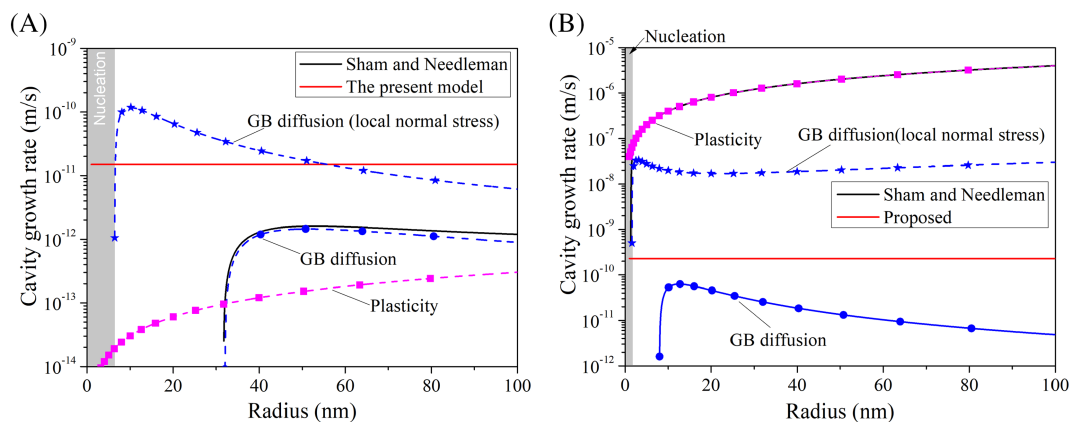


**FIGURE 14** The cavity-growth rate for small cavities calculated by the Sham and Needleman model in comparison with the present model at 500°C under the far-field applied stress of (A) 50 and (B) 200 MPa [Colour figure can be viewed at wileyonlinelibrary.com]

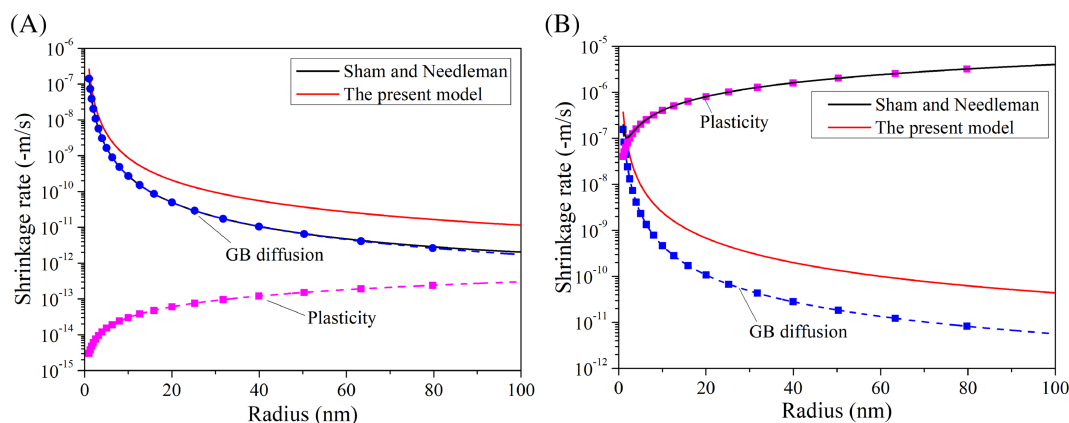


**FIGURE 15** The cavity shrinkage rate for small cavities calculated by the Sham and Needleman model in comparison with the present model at 500°C under the far-field stress of (A) -50 and (B) -200 MPa [Colour figure can be viewed at wileyonlinelibrary.com]

growth rate under both the 50 and 200 MPa far-field stress levels.

The prediction results using the  $\sigma_n$  instead of  $\sigma_s$  by the Sham and Needleman model are shown by the blue dashed line with stars. Growth occurs at a critical radius  $r_c$ , below which the cavity is still in the nucleation stage, as shown in hatched region in Figure 14. In the early stage (cavity radius of less than  $\sim 50$  nm; Figure 14A), the growth rate controlled by GB diffusion is higher than that of the surface diffusion. Since cavities likely occur at the location with local stress concentration,<sup>54</sup> it is possible that the GB diffusion is influenced by  $\sigma_n$ . Therefore, it is reasonable to consider that the newly nucleated cavities with small size would grow under the mechanism of surface diffusion as adopted in our present model, that is, Equations 4 and 5. For high stress level (Figure 14B), the growth rate predicted by using the Sham and Needleman model (plasticity controlled growth mechanism) is extremely high ( $>1 \mu\text{m s}^{-1}$ ), having a positive correlation between the cavity size and growth rate. This means that the cavity should become visible during experiment. But

metallographic observations seem to suggest that the damage induced under high stress level is characterized by transgranular crack with little creep cavitation.<sup>1</sup> In addition, an in situ nanotomography observation of cavitation process in Al-Cu alloy<sup>58</sup> suggested a nearly constant growth rate during creep. This provides an experimental verification to our present modeling observation (red line in Figure 14). Therefore, prediction of the early-stage cavity growth using Equations 4 and 5 might be a better option than the coupled diffusion and plasticity models developed for late-stage cavity growth.

Figure 15 compares the cavity shrinkage rates calculated by using the Sham and Needleman model with those calculated using the present shrinkage model (Equation 6), under compression stresses of -50 and -200 MPa, respectively. For both far-field stress levels, our proposed model shows a similar trend in comparison with the GB diffusion part of the Sham and Needleman model. This is as expected because both models are based on the GB diffusion mechanism. The proposed model gives a higher shrinkage rate as the  $\sigma_n$  instead of  $\sigma_s$  has

been used. It is interesting to note that the plasticity controlled mechanism becomes predominant from the cavity size as small as  $\sim 2$  nm and under high stress level of  $-200$  MPa (Figure 15B). By contrast, the effect of plasticity has not been incorporated in the present cavity shrinkage model.

To summarize, the employed cavity-growth models have more solid theoretical foundation than the coupled model while addressing the early-stage growth and shrinkage of newly nucleated cavities. However, they are valid only if the cavity radius is smaller than a certain size. This critical cavity size is different for the growth and shrinkage models, as they have been developed following two different cavity-growth mechanisms. The critical cavity radius for the growth model is positively correlated to the far-field stress, while a negative correlation exists for the cavity shrinkage model. Considering that the local normal stress relaxes quickly after the load reversal, the critical radius predicted by using both the growth and shrinkage models could be even smaller than the results presented in Figures 14 and 15. This indicates that the early-stage cavity growth and shrinkage processes for the nucleated cavities under creep-fatigue can be completed within one creep hold.

## 5 | CONCLUSIONS

A mechanistic-based cavitation model that considers nucleation, early-stage growth and sintering under multi-cycle creep-fatigue interaction has been developed for Type 316 stainless steel. The model replies on the local normal stress to connect the three concurrent or sequential cavitation events, providing important insights about how to design the creep-fatigue load waveform so that the creep cavitation can be enhanced. The following conclusions can be reached:

1. When tensile hold time is longer than that of compression, the creep-fatigue test with initial compression is advantageous in terms of creating more cavities.
2. Unbalanced stress hold time in favor of compression most likely closes all of the cavities nucleated during the previous tension phase.
3. Effect of compressive hold time or stress level on the number density of cavities in creep-fatigue tests is not monotonic. The underlying mechanism is their competing effect on nucleation and sintering.
4. There is an optimum value for the stress variation rate to obtain the highest number density of cavities, and their presence can be attributed to sintering effect.

5. Our model can satisfactorily explain several interesting experimental observations, including nucleation incubation time, effective nucleation field in a stress-frequency space for high-temperature fatigue, and the effect of unequal ramp rate on cavitation.

## 6 | FUTURE PERSPECTIVE

The classical nucleation theory that is widely used by the creep community was originated from the work that describes the formation of droplets in a vapor.<sup>62</sup> This implies the analogy between the two phenomenon, without detailed considerations whether it is justifiable or not. There are two drawbacks of the classical nucleation theory for creep cavitation; it tends to show a relatively weak temperature dependency while a much stronger stress dependency, when compared with experimental observations. The problem with classical nucleation theory could be eliminated if the nucleation is related to plastic strain. To this end, it is important to draw the readers' attention to our cavity nucleation model under creep-fatigue (eq. 25 in Hu et al.<sup>19</sup>), which predicts a positive correlation between the number density of cavities and creep strain. All initiatives towards cavitation modeling under the creep-fatigue conditions are encouraged, given that there is almost complete lack of fundamental understanding.

Regarding the classical nucleation theory, one should bear its limitation in mind. As demonstrated in the present cavitation model which is based on the classical nucleation theory, the predicted number density is in the order of magnitude of  $10^{-9}$  mm<sup>-2</sup>. Such a small number is likely due to the fact that nucleation rate (hence cavity density) is strongly dependent on the input material parameters (some physical parameters have not been experimentally measured yet).<sup>19,40</sup> One could take some steps to adjust the values of those material parameters so that the quantitative accuracy of the model output can be improved (e.g., a phenomenological model  $\dot{\rho} = B \cdot \dot{\epsilon}_{cr}$  with the  $B$  parameter adopted from He and Sandström<sup>63</sup>). However, this would certainly sacrifice the physical soundness of the model.

## ACKNOWLEDGMENTS

Bo Chen acknowledges financial supports by the UK's Engineering and Physical Sciences Research Council, EPSRC Early Career Fellowship Scheme (EP/R043973/1) and East China University of Science and Technology through the Ministry of Education of the People's Republic of China "the 111 Project." Jingdong Hu is funded partly by China Scholarship Council (CSC)



(201906740075) through the PhD Exchange Scheme. Bo Chen extends his sincere gratitude to Prof Shan-Tung Tu for providing academic mentorship and endless support.

## AUTHOR CONTRIBUTIONS

**Jingdong Hu:** Investigation, Data curation, Formal analysis, Writing - original draft, Visualization. **Changjun Liu:** Resources, Supervision, Writing - review & editing. **Fuzhen Xuan:** Supervision, Writing - review & editing, Funding acquisition. **Bo Chen:** Conceptualization, Methodology, Supervision, Writing - review & editing, Funding acquisition.

## DATA AVAILABILITY STATEMENT

Data sharing is not applicable to this article as no datasets were generated or analyzed during the current study.

## ORCID

Bo Chen  <https://orcid.org/0000-0003-1960-080X>

## REFERENCES

- Hales R. A quantitative metallographic assessment of structural degradation of type 316 stainless steel during creep-fatigue. *Fatigue Fract Eng Mater Struct.* 1980;3(4):339-356.
- Murty KL, Charit I. Structural materials for Gen-IV nuclear reactors: challenges and opportunities. *J Nucl Mater.* 2008; 383(1-2):189-195.
- Kassner ME, Hayes TA. Creep cavitation in metals. *Int J Plast.* 2003;19(10):1715-1748.
- Skelton RP, Gandy D. Creep-fatigue damage accumulation and interaction diagram based on metallographic interpretation of mechanisms. *Mater High Temp.* 2008;25(1):27-54.
- Rodriguez P, Rao KBS. Nucleation and growth of cracks and cavities under creep-fatigue interaction. *Prog Mater Sci.* 1993; 37(5):403-480.
- Davanas K. Determination of creep cavity nucleation rates. *Mater High Temp.* 2020;37(2):75-80.
- Nam SW. Assessment of damage and life prediction of austenitic stainless steel under high temperature creep-fatigue interaction condition. *Mater Sci Eng A.* 2002;322(1-2): 64-72.
- Cailletaud G, Nouailhas D, Grattier J, et al. A review of creep-fatigue life prediction methods: identification and extrapolation to long term and low strain cyclic loading. *Nucl Eng Des.* 1984; 83(3):267-278.
- Wen J-F, Srivastava A, Benzerga A, Tu S-T, Needleman A. Creep crack growth by grain boundary cavitation under monotonic and cyclic loading. *J Mech Phys Solids.* 2017;108: 68-84.
- Barbera D, Chen H, Liu Y. Advances on creep-fatigue damage assessment in notched components. *Fatigue Fract Eng Mater Struct.* 2017;40(11):1854-1867.
- Wilkinson DS. *The Mechanisms of Pressure Sintering.* University of Cambridge; 1978.
- Stevens RA, Flewitt PEJ. The sintering of creep-induced cavities in a low alloy ferritic steel (1Cr1Mo0.75V). *Metall Trans A.* 1983;14(3):679-686.
- Greenwood JN. Intercrystalline cracking of metals. *J Iron Steel Inst.* 1952;171:380-380.
- Raj R, Ashby MF. Intergranular fracture at elevated temperature. *Acta Metall.* 1975;23(6):653-666.
- Evans HE. *Mechanisms of Creep Fracture.* Elsevier Applied Science; 1984:319.
- Chen CW, Machlin ES. On a mechanism of high temperature intercrystalline cracking. *JOM.* 1957;9(7):829-835.
- Dunand DC, Han BQ, Jansen AM. Monkman-grant analysis of creep fracture in dispersion-strengthened and particulate-reinforced aluminum. *Metall Mater Trans A.* 1999;30(13): 829-838.
- Min BK, Raj R. Hold-time effects in high-temperature fatigue. *Acta Metall.* 1978;26(6):1007-1022.
- Hu J-D, Xuan F-Z, Liu C-J, Chen B. Modelling of cavity nucleation under creep-fatigue interaction. *Mech Mater.* 2021;156: 103799.
- Cocks ACF. Inelastic deformation of porous materials. *J Mech Phys Solids.* 1989;37(6):693-715.
- Cocks ACF, Ashby MF. Creep fracture by coupled power-law creep and diffusion under multiaxial stress. *Met Sci.* 1982; 16(10):465-474.
- Needleman A, Rice JR. Plastic creep flow effects in the diffusive cavitation of grain boundaries. *Acta Metall.* 1980;28(10): 1315-1332.
- Chuang T-J, Kagawa KI, Rice JR, Sills LB. Non-equilibrium models for diffusive cavitation of grain interfaces. *Acta Metall.* 1979;27(3):265-284.
- Chen I-W, Argon AS. Diffusive growth of grain-boundary cavities. *Acta Metall.* 1981;29(10):1759-1768.
- Chen I-W. Mechanisms of cavity growth in creep. *Scr Metall.* 1983;17(1):17-22.
- Miller DA, Hamm CD, Phillips JL. A mechanistic approach to the prediction of creep-dominated failure during simultaneous creep-fatigue. *Mater Sci Eng.* 1982;53(2):233-244.
- Tahir F, Liu Y. A new experimental testing method for investigation of creep-dominant creep-fatigue interaction in Alloy 617 at 950 °C. *Int J Press Vessels Pip.* 2017;154: 75-82.
- Fournier B, Sauzay M, Caes C, et al. Creep-fatigue-oxidation interactions in a 9Cr-1Mo martensitic steel. Part I: effect of tensile holding period on fatigue lifetime. *Int J Fatigue.* 2008;30(4): 649-662.
- Chen B, Flewitt PEJ, Cocks ACF, Smith DJ. A review of the changes of internal state related to high temperature creep of polycrystalline metals and alloys. *Int Mater Rev.* 2015;60(1): 1-29.
- Frost HJ, Ashby MF. *Deformation Mechanism Maps: The Plasticity and Creep of Metals and Ceramics.* Pergamon Press; 1982.
- Mortimer DA, Nicholas MG. Surface and grain-boundary energies of AISI 316 stainless steel in the presence of boron. *Met Sci.* 1976;10(9):326-332.
- Wang JS, Stephens JJ, Nix WD. A statistical analysis of cavity nucleation at particles in grain boundaries. *Acta Metall.* 1985; 33(6):1009-1021.



33. Stroth AN. A theory of the fracture of metals. *Adv Phys.* 1957; 6(24):418-465.
34. Nix WD, Yu KS, Wang JS. The effects of segregation on the kinetics of intergranular cavity under creep conditions. *Metall Trans A.* 1983;14(3):563-570.
35. Riedel H. *Fracture at High Temperatures.* Springer; 1987.
36. Fedelich B, Owen J. Creep damage by multiple cavity growth controlled by grain boundary diffusion. In: *12th International Conference on Fracture.* National Research Council Canada; 2009.
37. Chen B, Hu JN, Flewitt PEJ, et al. Effect of thermal ageing on creep and oxidation behaviour of Type 316H stainless steel. *Mater High Temp.* 2015;32(6):592-606.
38. ASME. *ASME BPVC III-Div.1 Subsection NH. Class 1 Components in Elevated Temperature Service.* ASME; 2015.
39. Chen B, Flewitt PEJ, Smith DJ, Jones CP. An improved method to identify grain boundary creep cavitation in 316H austenitic stainless steel. *Ultramicroscopy.* 2011;111(5):309-313.
40. Raj R. Nucleation of cavities at second phase particles in grain boundaries. *Acta Metall.* 1978;26(6):995-1006.
41. Fleck RG, Taplin DMR, Beevers CJ. An investigation of the nucleation of creep cavities by 1 MV electron microscopy. *Acta Metall.* 1975;23(4):415-424.
42. Shi HJ, Pluvineau G. Cyclic stress-strain response during isothermal and thermomechanical fatigue. *Int J Fatigue.* 1994; 16(8):549-557.
43. Michel DJ, Smith HH. Accelerated creep-fatigue crack propagation in thermally aged type 316 stainless steel. *Acta Metall.* 1980;28(7):999-1007.
44. Ghafouri SN, Faulkner RG, Chung TE. Microstructural developments in type 316L stainless steel during low-cycle fatigue at 350–550°C and their effects on cyclic strength and life. *Mater Sci Technol.* 1986;2(12):1223-1232.
45. Taplin DMR, Tang NY, Leipholz HHE. On fatigue-creep-environment interaction and the feasibility of fatigue maps. In: *6th International Conference on Fracture.* Elsevier; 1984: 127-142.
46. Tang NY, Taplin DMR, Plumtree A. Schema for depicting cavity nucleation during hightemperature fatigue. *Mater Sci Technol.* 1985;1(2):145-151.
47. Yamaguchi K, Kanazawa K. Effect of strain wave shape on high temperature fatigue life of a type 316 steel and application of the strain range partitioning method. *Metall Trans A.* 1980; 11(12):2019-2027.
48. Morin L, Leblond J-B, Benzerga AA, Kondo D. A unified criterion for the growth and coalescence of microvoids. *J Mech Phys Solids.* 2016;97:19-36.
49. Cocks ACF, Ashby MF. Intergranular fracture during power-law creep under multiaxial stresses. *Met Sci.* 1980;14(8-9): 395-402.
50. Hu J-D, Xuan F-Z, Liu C-J. A void growth model of multiaxial power-law creep rupture involving the void shape changes. *Int J Mech Sci.* 2018;144:723-730.
51. Sanders JW, Dadfarnia M, Stubbins J, Sofronis P. On the fracture of high temperature alloys by creep cavitation under uniaxial or biaxial stress states. *J Mech Phys Solids.* 2017;98:49-62.
52. Wilson D, Wan W, Dunne FPE. Microstructurally-sensitive fatigue crack growth in HCP, BCC and FCC polycrystals. *J Mech Phys Solids.* 2019;126:204-225.
53. Wilson D, Dunne FPE. A mechanistic modelling methodology for microstructure-sensitive fatigue crack growth. *J Mech Phys Solids.* 2019;124:827-848.
54. Jirandehi AP, Khonsari MM. General quantification of fatigue damage with provision for microstructure: a review. *Fatigue Fract Eng Mater Struct.* 2021;44(8):1973-1999.
55. Raj R, Ashby MF. Intergranular fracture at elevated temperature. *Acta Metall.* 1975;23(6):653-666.
56. Needham NG, Gladman T. Nucleation and growth of creep cavities in a Type 347 steel. *Met Sci.* 1980;14(2):64-72.
57. Rezgui B, Petrequin P, Mottot M. Hold time effects on low cycle fatigue properties of 316 L stainless steel at 600 °C and 650 °C. In: *Conférence internationale sur la rupture.* CEA Centre d'Etudes Nucleaires de Saclay; 1981.
58. Kumar R, Villanova J, Lhuissier P, Salvo L. In situ nanotomography study of creep cavities in Al-3.6-Cu alloy. *Acta Mater.* 2019;166:18-27.
59. Beere W, Speight MV. Creep cavitation by vacancy diffusion in plastically deforming solid. *Met Sci.* 1978;12(4):172-176.
60. Margolin BZ, Gulenko AG, Kursevich IP, Buchatskii AA. Modeling for fracture in materials under long-term static creep loading and neutron irradiation. Part 1. A physico-mechanical model. *Strength Mater.* 2006;38(3):221-233.
61. Sham TL, Needleman A. Effects of triaxial stressing on creep cavitation of grain boundaries. *Acta Metall.* 1983;31(6): 919-926.
62. Dean RB. The formation of bubbles. *J Appl Phys.* 1944;15(5): 446-451.
63. He J, Sandström R. Formation of creep cavities in austenitic stainless steels. *J Mater Sci.* 2016;51(14):6674-6685.

**How to cite this article:** Hu J, Liu C, Xuan F, Chen B. Modeling of cavity nucleation, early-stage growth, and sintering in polycrystal under creep-fatigue interaction. *Fatigue Fract Eng Mater Struct.* 2022;45(3):882-903. doi:10.1111/ffe.13643

## APPENDIX A: EQUATIONS FOR DERIVING THE LOCAL NORMAL STRESS IN EQUATION 2

To derive Equation 2 for the local normal stress  $\sigma_n$ , let us consider the “spring-dashpot” framework adopted in the Chen–Hu model<sup>19</sup> (Figure A1). The left arm describes the stress applied on a grain boundary (GB), and the right arm describes the stress applied on the neighboring grains.

The local normal stress  $\sigma_n$  is equivalent to the stress concentration at GB particles, which gives

$$\sigma_n = \frac{\eta_b}{f_b} \cdot \dot{U}_{sb}, \quad (\text{A1})$$

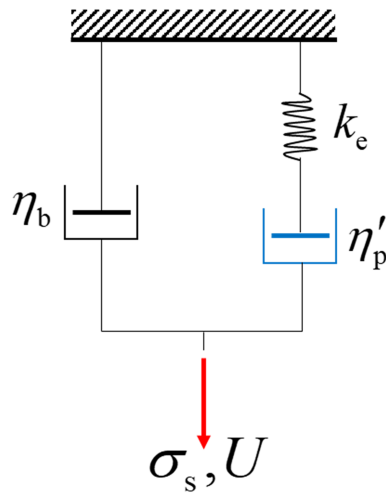


**FIGURE A1** Spring-dashpot model<sup>19</sup> [Colour figure can be viewed at [wileyonlinelibrary.com](http://wileyonlinelibrary.com)]

where  $\dot{U}_{sb}$  is the GB sliding rate.  $\eta_p$  is damping coefficient for the Norton power-law creep with the deformation rate  $\dot{U}_{cr}$  as formulized below:

$$\dot{U}_{cr} = \frac{1}{\eta_p \cdot \sigma_{sa}^{n-1}} \sigma_{sa} = \frac{1}{\eta_p} \sigma_{sa}, \quad (\text{A2})$$

where  $\sigma_{sa}$  is the stress shared in the neighboring grains. An intermediate parameter, transient damping coefficient  $\eta'_p$ , has been introduced to reduce the complexity when calculating the  $\dot{U}_{cr}$ . Then,  $\eta'_p$  at the next time  $t + \Delta t$  can be calculated by  $\sigma_s(t + \Delta t)$  and  $\sigma_n(t)$  from previous time  $t$ :

$$\lim_{\Delta t \rightarrow 0} \eta'_p(t + \Delta t) = \eta_p / [\sigma_s(t + \Delta t) - f_b \sigma_n(t)]^{n-1}. \quad (\text{A3})$$

For a sufficiently small time increment  $\Delta t$ ,  $\eta'_p$  can be approximated as a constant. Thus, the differential equation for  $\sigma_n$  can be derived as

$$\dot{\sigma}_n + k_e \left( \frac{1}{\eta_b} + \frac{1}{\eta'_p} \right) \sigma_n = \frac{1}{f_b} \left( \dot{\sigma}_s + \frac{k_e}{\eta'_p} \sigma_s \right). \quad (\text{A4})$$

Basically, Equation 2 is the solution of Equation A4, and that explicit form is more convenient for numerical calculations.

## APPENDIX B: SURFACE DIFFUSION FACTOR $D_S$ AND THE DERIVATION OF EQUATION 4

Free surface diffusion coefficient  $D_S$  is used only in Equation 4 to describe the crack-like cavity-growth rate via the diffusivity ratio of  $\delta_s D_S / \delta D_B = 0.001$ . The condition that determines the low or high stress, as reported in Nix et al.,<sup>34</sup> is formulized as

$$\dot{r} = \begin{cases} \frac{\Omega \delta_s D_S}{2kT\gamma^2} \sigma_n^3, & \sigma_n \leq \frac{\gamma}{3.5b} \left( \frac{\delta D_B}{\delta_s D_S} \right), \\ \frac{(\delta D_B)^{3/2} \Omega \sigma_n^{3/2}}{2(\delta_s D_S)^{1/2} kTb^{3/2} \gamma^{1/2}}, & \sigma_n > \frac{\gamma}{3.5b} \left( \frac{\delta D_B}{\delta_s D_S} \right). \end{cases} \quad (\text{B1})$$

A sensitivity study was conducted at 550°C to examine the effect of the  $\delta_s D_S / \delta D_B$  value selection on the cavity-growth rate. Figure B1 shows the calculated relationship between the local normal stress  $\sigma_n$  and cavity-growth rate  $\dot{r}$  by using different  $\delta_s D_S / \delta D_B$  values. Only the  $\delta_s D_S / \delta D_B$  values of less than 1 need to be considered for the crack-like cavity growth.<sup>34</sup> Within the stress range of 100 to 1000 MPa, the calculated curve with  $\delta_s D_S / \delta D_B = 0.001$  (in red) shows the highest cavity-growth rate, Figure B1. The solid curves as predicted using Equation B1 are not continuous. A modification was made to the function (see Equation 4), to provide a continuous curve prediction (the dashed curve). The stress range highlighted by red box indicates the magnitude

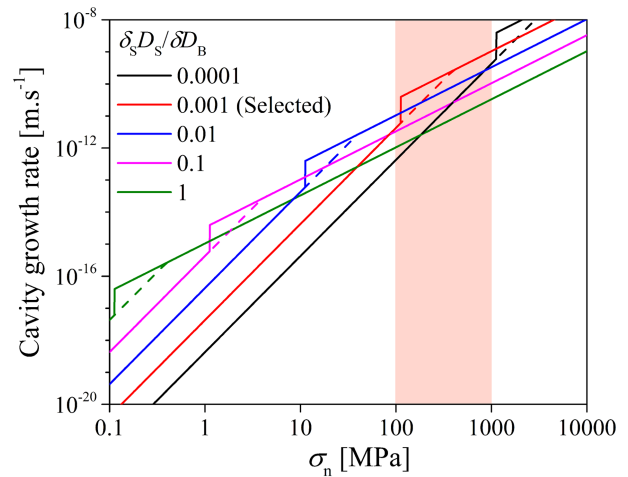


**FIGURE B1** Effect of diffusivity ratio  $\delta_s D_S / \delta D_B$  on the cavity-growth rate. Dashed curves were predictions using Equation 4, while solid curves were based on Equation B1 [Colour figure can be viewed at [wileyonlinelibrary.com](http://wileyonlinelibrary.com)]

facilitating the cavity growth, according to Figures 5 and 6. For the maximum cavitation under creep-fatigue,  $\delta_S D_S / \delta D_B = 0.001$  has thus been selected to derive the value of  $D_S$ .

### APPENDIX C: NUMERICAL ERROR

The forward Euler method creates a limited numerical calculation error, if the time interval  $\Delta t$  is small enough. This method has been used in previous work on cavitation, for example, Sanders et al.<sup>51</sup> and Margolin et al.<sup>60</sup> Figure C1 presents calculation results on the basis of different  $\Delta t$  values. It is clear that  $\Delta t = 0.5$  s generates a marginal difference (less than 2.5%) when compared with those using any smaller values (e.g.,  $\Delta t = 0.1, 0.05$  s). Thus, the selection of  $\Delta t = 0.5$  is justified.

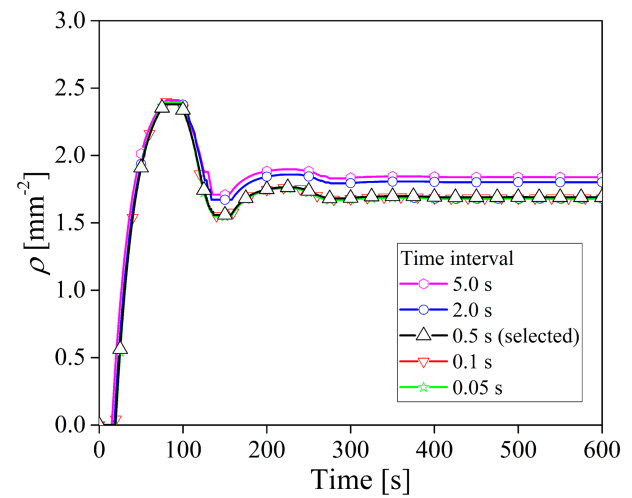


**FIGURE C1** Effect of  $\Delta t$  value on the numerical calculation results  $\Delta t = 0.5$ , under the condition of  $550^\circ\text{C}$ , stress amplitude of 200 MPa with initial tension, zero mean stress, and tensile hold time of 60 s [Colour figure can be viewed at [wileyonlinelibrary.com](https://onlinelibrary.wiley.com)]